Experimental Investigation and Fundamental Understanding of a Slowed UH-60A Rotor at High Advance Ratios

Anubhav Datta
Science and Technology Corporation

Hyeonsoo Yeo
Aeroflightdynamics Directorate (AMRDEC)
U.S. Army Research Development and Engineering Center

Thomas R. Norman
Aeromechanics Branch, NASA

NASA Ames Research Center, Moffett Field, CA

ABSTRACT

This paper describes and analyzes the measurements from a full-scale, slowed RPM, UH-60A rotor tested at the National Full-Scale Aerodynamics Complex 40- by 80- ft wind tunnel up to an advance ratio of 1.0. A comprehensive set of measurements, that includes performance, blade loads, hub loads and pressures/airloads makes this data set unique. The measurements reveal new and rich aeromechanical phenomena that are special to this exotic regime. These include reverse chord dynamic stall, retreating side impulse in pitch-link load, large inboard-outboard elastic twist differential, supersonic flow at low subsonic advancing tip Mach numbers, diminishing rotor forces yet dramatic build up of blade loads, and dramatic blade loads yet benign levels of vibratory hub loads. The objective of this research is the fundamental understanding of these unique aeromechanical phenomena. The intent is to provide useful knowledge for the design of high speed, high efficiency, slowed RPM rotors of the future and a challenging database for advanced analyses validation.

NOMENCLATURE

$C_{D,A,H}$	rotor drag; nondim. by $\rho\pi R^2(\Omega R)^2$
$C_{L,N,T}$	rotor thrust; nondim. by $\rho\pi R^2(\Omega R)^2$
C_{DE}	effective drag coeff.
	$C_{DE} = (C_{Pi} + C_{Po})/\mu = C_P/\mu - C_X$
	$C_{DE} = -C_X$ in autorotation
C_{Ho}	profile H-force coeff.
C_P	power coeff. $= P/\rho A(\Omega R)^3 = C_Q$
	$C_P = C_{Pi} + C_{Po} + \mu C_X$
C_{Pi}	induced power coeff.
C_{Po}	profile power coeff. $= C_{Qo} + \mu C_{Ho}$
C_Q	torque coeff. $= Q/\rho\pi R^2(\Omega R)^2 R = C_P$
C_{Qo}	profile torque coeff.
C_X	propulsive force coeff.$= -C_D$
C_p	pressure coeff. $= 2(p - p_\infty)/\rho U_\infty^2$
C_p^*	sonic pressure coeff.
	$C_P = C_P^*$ when $M_l = 1.0$
D, A, H	rotor drag in wind, horiz. and shaft axes
L, N, T	rotor thrust in wind, vert. and shaft axes
L/D_E	lift-to-drag ratio $= C_L/C_{DE}$
M_A	advancing tip Mach number
M_T	tip Mach number $= \Omega R/a$
M_l	surface Mach number
M^2c_c	chord force distribution
	nondim. by $\frac{1}{2}\rho a^2 c$
M^2c_m	1/4-c pitch. mom. distribution
	nondim. by $\frac{1}{2}\rho a^2 c^2$
M^2c_n	normal force distribution
	nondim. by $\frac{1}{2}\rho a^2 c$
P, Q	rotor power, torque; $P = \Omega Q$

Presented at the American Helicopter Society 66th Annual Forum, Virginia Beach, VA, May 3–5, 2011.

R	rotor radius
V	tunnel speed
X	propulsive force $= -D$
a	speed of sound
c	local chord
c_l, c_d	sectional lift and drag coeffs.
r	radial station
Ω	rotor RPM
$\Delta\alpha$	tunnel correction angle, +ve in up wash
α_S	shaft angle, +ve aft
μ	advance ratio $V/\Omega R$
ρ	density
γ	heat capacity; 1.4 for air at 20°C
σ	rotor solidity; 0.0826
θ_{75}	collective angle at 75% R, degree
θ_{1S}, θ_{1C}	longitudinal and lateral cyclics, degree

INTRODUCTION

Slowed rotors are recognized as technology enablers for higher speeds in edgewise rotors and higher cruise efficiencies in tiltrotors. Even at low speeds, optimal use of rotor speed can offer significant efficiency gains, assuming a required thrust level can be maintained. As a result, considerable attention is devoted today towards the development of wide speed-range power turbines and continuously variable multiple-speed transmissions for rotorcraft [1, 2]. Some of these technologies are already available today in limited form, and have found application on advanced rotorcraft. For instance, a 15-20% reduction in engine RPM is deliverable by today's commercial power turbines with no more than 5-10% penalty in specific fuel consumption [3]. The Sikorsky X2 Technology Demonstrator slows its rotor by 20% from 446 to 360 revolutions per minute (RPM) to fly at 250 kt using a similar technology [4, 5]. The Bell/Boeing V-22 Osprey slows its rotor by 19% from 412 to 333 RPM to fly in cruise using a similar technology. Two-speed transmissions, with innovative gear-boxes and clutches for changing gears in flight, have also been demonstrated. Frontier System's optimum speed rotor – now part of Boeing's 6500 lb A160 unmanned air vehicle (UAV) – uses a similar technology on edgewise rotors for high efficiency low speed flight [6]. It is now being pursued on tiltrotors for high efficiency high speed flight [7]. Even though the underlying technology of RPM reduction remains the same in both edgewise rotors and tiltrotors, the aeromechanics of their operations is entirely different. An edgewise rotor, when slowed down for the purposes of high speed, begins to operate at very high, non-conventional advance ratios (μ= 0.7 – 1.0 and beyond). About 80% or more of its retreating side now remains immersed in reverse flow. The objective of this research is to understand the aeromechanics of such a slowed rotor.

High advance ratios are traditionally associated with autogiros [8] or innovative helicopter-autogiro hybrids [9, 10]. For a helicopter to achieve high speeds (200-300 kt) and yet remain efficient and maneuverable, it is desired that the rotor be powered and remains controlled. The word slowed rotor refers to such rotors. By definition, slowed rotors generate lower forces and moments, and are therefore intended primarily for use in compound helicopters (with the exception of lightweight UAVs). The decades of 1960s - 70s saw extensive research, development and flight testing of a wide variety of compound helicopters [11, 12]. The developments spurred significant research on high advance ratio slowed rotors, yet, none actually found a place on an aircraft at the time. Some of the aircraft, like the U.S. Army XH-51A (Lockheed), experimented with RPM reduction but only down to 95% nominal, below which structural resonance problems were encountered [13]. Eventually, none of these aircraft entered regular production. Today, with advances in materials, controls, and engine/drivetrain technologies, compounds have once again emerged as potential contenders for high-speed heavy lift rotorcraft [14] – this time, envisioned to be equipped with slowed rotors. One vision for the future is a 50% or more reduced RPM slowed rotor that is applicable to heavy lift, high speed, high efficiency rotorcraft.

Extensive analytical investigations of slowed rotors were performed in the last decade [15–19]. Successful flight demonstrations of three modern compound helicopters were also carried out, namely: the Sikorsky X2 with a coaxial rotor and pusher prop [20], the Eurocopter X^3 with a wing and two wing mounted propellers [21, 22], and the Piasecki X-49A with a wing and a Vectored Thrust Ducted Propeller [23]. The coaxial X2 flew at advance ratio of $\mu = 0.8$ at 80% nominal RPM (hover) to demonstrate successful flight at 250 kt. The single rotor X^3 demonstrated 180 kt with the eventual goal of reaching 220 kt at advance ratio of $\mu = 0.66$ at 78% nominal RPM. Additionally, CarterCopter's successful demonstration of the first ever $\mu = 1.0$ flight in 2005 with 50% reduced RPM, even though as an autogiro, contributed further to growing interest in high advance ratio slowed rotors [24].

A slowed rotor must operate as a conventional rotor in hover and yet all but disappear – in drag, loads and vibration – at high speeds. Understanding their fundamental dynamics is important to address this technical challenge efficiently (minimum vehicle power) and safely (control reversal, loads and vibration, stability). Unlike conventional rotors, there is a scarcity of experimental data and a lack in the fundamental understanding of the aerodynamic and dynamic environment of high advance ratio slowed rotors. Historically, only four full-scale high advance ratio tests are documented: the Pitcairn PCA-2 Autogiro tests in the NACA Langley 30- by 60- ft wind tunnel [25], a two-bladed teetering rotor test at the same tunnel [26, 27],

the Sikorsky H-34 tests in the NASA Ames 40- by 80-ft wind tunnel [28], and the Bell UH-1 tests in the same wind tunnel [29]. All of these tests, conducted during the 1960s (the autogiro test was in 1930s), provide only rotor performance and blade root motions and limited flow visualization (tufts). Recently, a comprehensive study was conducted on correlating these data with analyses [30]. The study highlighted the discrepancies in current analyses – both lifting-line and CFD based – in predicting high advance ratio performance. These discrepancies have not been addressed systematically due to the scarcity of reliable and comprehensive test data. Several researchers are carrying out model-scale tests in recent years to address the above technical challenges [31, 32]. The focus of the present research is on full-scale testing.

In an effort to address the lack of fundamental understanding as well as comprehensive data, a full-scale UH-60A rotor (26.83 ft radius, 4-bladed, fully articulated) was tested at the U. S. Air Forces' National Full-Scale Aerodynamics Complex (NFAC) 40- by 80-ft wind tunnel at slowed rotational speeds - 65% and 40% of nominal – with resultant advance ratios reaching up to 1.0. A comprehensive set of measurements including performance, blade loads, hub loads and pressures/airloads make this data set unique. The test was part of a broader UH-60A airloads test program [33]. The program was divided into six test phases. The first five phases involved conventional operations: 1-g level flight speed sweeps, parametric sweeps, reproduction of earlier flight test and DNW tunnel test points, and Particle Image Velocimetry (PIV) tests. The fifth phase was the high advance ratio Slowed Rotor Test (SRT) – the subject matter of this paper. The objective was to explore the aeromechanics of a conventional (edgewise) rotor in a non-conventional (large reverse flow) regime in anticipation of the next generation of high speed, high efficiency, variable RPM rotors.

Finally, note that the UH-60A rotor was not designed to operate in a high advance ratio regime. It is precisely for this same reason, however, that it is expected to reveal many of the critical, limiting aeromechanical phenomena that will constrain the design and operation of future slowed rotors in this regime.

Scope of Paper

The present test differs from those conducted earlier in that it acquires a more complete set of measurements: performance, motions, structural loads, hub loads and pressures/airloads under slowed RPM high advance ratio conditions. The emphasis of this paper is on the fundamental understanding of aeromechanics in this unique regime by connecting flow phenomena to rotor performance and structural loads. The first section provides a brief description of the experiment, emphasizing the special considerations of the slowed rotor test. The second section describes the test points. The following three sections examine specific results from this test: performance, structural loads and hub loads, and pressure and airloads.

Figure 1: **Full-scale UH-60A rotor installed on the Large Rotor Test Apparatus in the NFAC 40- by 80- ft wind tunnel.**

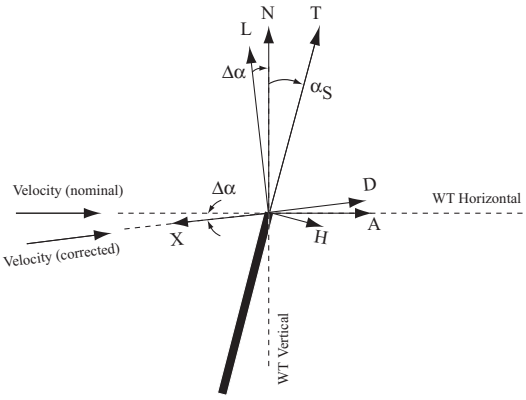

Figure 2: **Model shaft angle α_S, wall correction $\Delta\alpha$, and rotor forces in tunnel axes (N and A), shaft axes (T and H), and corrected wind axes (L and D), and the propulsive force (X = -D).**

DESCRIPTION OF EXPERIMENT

The hardware, measurement systems, data acquisition systems, data reduction procedures, and pre-test activities common to all six test phases are described in detail in Ref. [33]. A brief summary is provided here, with details relevant to and considerations specific to this test.

Model: The UH-60A rotor mounted on the NFAC Large Rotor Test Apparatus (LRTA) is shown in Fig. 1. A schematic of the model defining the force conventions is given in Fig. 2. The tunnel wall correction $\Delta\alpha$, based on the rotor diameter to tunnel width ratio, model offset from center-line (10.9 inches up), and rotor disk area to tunnel area (79 ft x 39 ft, 1 ft reduced for acoustic

lining) ratio, is given by

$$\Delta\alpha = 8.6101\left(C_N/\mu^2\right) \quad \text{deg} \tag{1}$$

Instrumentation: The blades are exactly the same four blades flown during the 1993 Airloads Program [34], but refurbished and re-calibrated with new instrumentation. A total of 332 rotor and hub measurements and 124 LRTA and wind tunnel measurements were acquired during the test. The rotor and hub measurements included: a total of at least 160 working pressure transducers (down from 215 functional transducers at the beginning of test, out of 235) arranged chordwise and spanwise in Gaussian spacing over nine stations (22.5, 40, 55, 67.5, 77.5, 86.5, 92, 96.5, and 99% R) and several additional intermediate stations; a total of 26 two- or four-leg strain-gage bridges on a second instrumented blade for structural loads at the root (11.3%R) and eight uniformly distributed stations from 20% to 90%R; two independent blade motion hardware – a set of three Rotary Variable Differential Transformers (RVDTs) mounted on each blade hinge points and a set of three laser distance transducers mounted on each blade hub arm; 8 strain gage bridges on the shaft – 4 to measure shaft stresses and 4 to measure shaft bending moments; and 10 four-leg strain-gage bridges to measure axial loads on the pitch links (4), damper (4), and rotating scissors (2). The LRTA and wind tunnel measurements included: a five-component rotor balance – four flexures instrumented with 12 primary and 12 back-up gages for three forces and pitching and rolling moments, and an in-line flex-coupling for torque; 8 strain-gage bridges to measure non-rotating control system forces and moments (3 bridges on stationary pushrods, one bridge on stationary scissor, and 4 on the swashplate guide); 6 displacement measurements of the primary (3) and dynamic (3) actuators; 6 load cells between LRTA fairing and chassis for steady fuselage loads; and 31 tunnel pressure/temperature measurements, 3 model angle measurements and a rotor RPM measurement. The blade pressure data were acquired at 2048 per revolution (/rev). The motions and loads data were acquired at 256/rev.

Independent measurements: In addition to the above, two independent data sets were acquired: spanwise blade deformations, using 8 CCD progressive scan cameras, 16 high-power xenon flash-lamp strobes on the test section floor cavities and 48 retro-reflective targets on the blade lower surfaces [35]; and density gradients downstream of the advancing blade to track tip vortices with retro-reflective background oriented schlieren, using 2 cameras synchronized to rotor 1/rev, a retro-reflective light source, and a speckled background put on the tunnel wall [36]. Data from these measurements are part of ongoing investigation and beyond scope of this paper.

Motion and loads allowables: Several special steps were taken for the slowed rotor test including those based on Sikorsky's review of the motions and loads allowables at reduced RPM. The main rotor dynamic flap and droop stop mechanisms were modified to allow adequate flapping at the reduced RPM. The lag displacement was monitored for instabilities in case 1–3/rev motions significantly decreased damping at the lag frequency. Trailing edge strains (vibratory and positive/negative peaks) at 50% R and 68% R were added as safety of flight parameters in case decreased centrifugal forcing led to compression from edgewise bending. The lug stress at the blade cuff was confirmed not to be a concern.

Test plan and procedure: The test plan was constructed as a parametric sweep with tip Mach number M_T as the primary variable. The M_T settings were 0.65 at 100% nominal RPM (NR) of 258, 0.42 at 65% NR and 0.26 at 40%NR. The maximum model speed was limited to 182 kt (maximum tunnel speed is 300 kt). The minimum RPM (40% NR) and the maximum model speed were set by safety of flight considerations. These limits determined the maximum advance ratio. All RPM changes were carried out after bringing the tunnel speed down to zero or a very low value (nominal hover), to prevent resonance due to changing blade frequencies. Similarly, all shaft angle changes were carried out after bringing the tunnel speed down, to avoid large transient blade flapping. The emergency shut down procedure was to reduce the tunnel speed first. The test procedure was: (1) set RPM (i.e., M_T); (2) set shaft angle α_S; (3) vary tunnel speed for intended μ; (4) at each μ, acquire data over a range of collective angles with the maximum limited by cyclic control limits or load limits whichever was encountered first (usually the latter); and (5) after completion of the collective sweeps at all μ, bring tunnel speed down, and go to next α_S. Each collective setting was a test point. At each test point, the rotor was trimmed to minimize flapping manually.

PERFORMANCE MEASURES

The following definitions are used for interpretation of performance.

Rotor power C_P equals rotor torque C_Q in coefficient form. Torque includes induced (c_l contribution) and profile (c_d contribution) components.

$$C_P = C_Q = C_{Qi} + C_{Qo} \tag{2}$$

Adding and subtracting $\mu C_H = \mu(C_{Hi} + C_{Ho})$, recognizing $C_{Qi} + \mu C_{Hi} = \int \lambda dC_T$, and defining profile power as $C_{Po} = C_{Qo} + \mu C_{Ho}$, Eq. 2 takes the form

$$C_P = \int \lambda dC_T + C_{Po} - \mu C_H \tag{3}$$

Table 1: **Slowed rotor test runs; NR: Nominal RPM (258), α_S: shaft angle (deg), V: speed (kt), μ: advance ratio, M_A: advancing tip Mach no., θ_{75}: collective angle (deg).**

Run	% NR	α_S	V	μ	M_A	θ_{75}
R66	100	0.0	130	0.3	0.85	-0.1–10.0
		2.0				0.0–9.9
		4.0				-0.1–5.9
R69		0.0	172	0.4	0.91	0.4–8.0
		2.0				-0.1–8.0
		4.0				0.0–5.9
R87	65	0.0	83	0.3	0.55	-0.1–7.9
			111	0.4	0.59	-0.1–7.9
			139	0.5	0.63	-0.1–7.9
			167	0.6	0.67	0.0–7.9
R91	40	0.0	52	0.3	0.34	0.0–8.0
			69	0.4	0.36	-0.1–8.0
			87	0.5	0.39	0.0–8.0
			104	0.6	0.42	0.0–7.9
			121	0.7	0.44	0.0–8.0
			139	0.8	0.47	-0.1–8.0
			157	0.9	0.49	0.0–4.0
			174	1.0	0.52	-0.8–1.8
R93		4.0	52	0.3	0.34	0.0–8.0
			70	0.4	0.36	0.0–8.0
			87	0.5	0.39	-0.1–8.0
			104	0.6	0.42	0.0–8.0
R95			52	0.3	0.34	0.9,1.1
			104	0.6	0.36	2.8,5.1,6.2
			121	0.7	0.44	-0.1–7.7
			138	0.8	0.47	-0.1–7.7
			156	0.9	0.49	-0.1–6.2
			173	1.0	0.52	0.0–2.0
R96		2.0	52	0.3	0.34	1.7,1.9
			70	0.4	0.36	1.9
			87	0.5	0.39	1.9
			104	0.6	0.42	2.0
			121	0.7	0.44	1.9
			139	0.8	0.47	1.9
			156	0.9	0.49	1.9
			174	1.0	0.52	0.9

Separating inflow into induced and forward speed components as $\lambda = \lambda_i - \mu(\alpha_s + \Delta\alpha)$, where α_s is positive for tilt back as per test convention, recognizing $(\alpha_s + \Delta\alpha)C_T + C_H = C_D = -C_X$ (see Fig. 2 and assume small angles), and defining induced power as $C_{Pi} = \int \lambda_i dC_T$, leads to the energy balance expression

$$C_P = C_{Pi} + C_{Po} + \mu C_X \tag{4}$$

μC_X is power for propulsion. Because the remainder is power associated entirely with lift generation, it is represented as an effective drag C_{DE} where $\mu C_{DE} = C_{Pi} + C_{Po}$. Thus effective drag is

$$C_{DE} = C_P/\mu - C_X \tag{5}$$

Rotor efficiency (lift to drag ratio) follows

$$L/D_E = \frac{C_L}{C_P/\mu - C_X} \tag{6}$$

In autorotation, $C_P = 0$, hence (from Eq. 5)

$$C_{DE} = -C_X. \tag{7}$$

SLOWED ROTOR TEST MATRIX

The slowed rotor test points are summarized in Table 1. There are a total of 232 points; 47 of these are a set of 100% NR points carried out at three shaft angles 0, 2, and 4°; 36 are a set of 65% NR points carried out at a single shaft angle of 0°; and 149 are a set of 40% NR points carried out at three shaft angles 0, 2, and 4°.

The 40% NR points constitute the more comprehensive of the two slowed RPM sets. The maximum advance ratio of $\mu = 1.0$ was achieved during this set. The points at shaft angle 2° were obtained only at a single collective, nominally 2°, except for the highest advance ratio of $\mu = 1.0$, where it was obtained additionally at 1°. The points at shaft angle 4° were obtained over two separate runs, 93 and 95. The first two points of run 95 (shown in grey) were check points repeating the first and last points from run 93.

The advance ratios and advancing tip Mach numbers matrix of the test points, Fig. 3, indicate a useful separation of high compressibility and high reverse flow physics. The largest variation of μ (i.e. extent of reverse flow) from 0.3 to 1.0 is contained entirely within the subsonic regime. Additional features of the test matrix design is described in Fig. 4 which presents a summary of all the test points in a power-speed envelope. There are two sets of points that have common speeds at different RPM. The speed 139 kt is a common speed between 65% and 40% NR (with $\mu = 0.5$ and 0.8 respectively). Similarly, the speed 174 kt is common between 100% and 40% NR (with $\mu = 0.4$ and 1.0 respectively). In other words, the nominal rotor at $\mu = 0.4$ flies at the same speed as the 40% NR rotor

at $\mu = 1.0$. The 65% NR rotor at $\mu = 0.5$ flies at the same speed as the 40% NR rotor at $\mu = 0.8$. There is a pair of points that represents a common advancing tip Mach number but widely different advance ratios – the 65% NR, μ=0.3 point and the 40% NR, μ=1.0 point.

The thrust-speed envelope is shown in Fig. 5. Thrust is minimal for the slowed rotor, as expected, but not insignificant (2000-3000 lb) at $\mu = 1.0$. Even though the dimensional thrust is low, the collective sweeps up to load limit ensured high non-dimensional thrust levels. The non-dimensional thrust-speed envelopes for shaft angles of 0° and 4° are shown in Figs. 6 and 7 respectively. The rotor generated drag at all points, but never operated in autorotation. The proximity of the test points to autorotation is shown in Fig. 8 where the effective drag coefficient is plotted along with the value expected during autorotation. It came closest to autorotation for the 40% NR case with a shaft angle of 4° at the highest advance ratios.

From the test matrix, test points for parametric sweeps are identified for the purposes of studying structural loads, hub loads and airloads. The first two digits of each test point identify the run number. Table 2 shows two RPM sweeps (i.e., M_T sweeps), at advance ratios of 0.3 and 0.4. These sweeps isolate the effects of slowing the rotor while keeping the reverse flow area the same. Table 3 shows two advance ratio sweeps at shaft angles 0° and 4°. The thrust level is the same between the two so that the two sets can also be used to study the effect of shaft angle variation. These sweeps isolate the effects of increasing reverse flow area. Note that the advance ratio sweep is also a speed sweep since all points are at the same RPM (40% NR). Table 4 shows six thrust sweeps – two sets each for shaft angles 0° and 4°, and each set constituting three collective sweeps at advance ratios 0.8, 0.9, and 1.0. The sweeps isolate the effects of reverse flow stall. Selected subsets of the above sweeps are used in this paper to illustrate the special aeromechanical phenomena of the high advance ratio regime.

Table 2: **Slowed rotor test points for RPM (i.e. M_T) sweeps at two different advance ratios; Pt: test point number, C_T/σ: nondim. thrust, θ_{1C} and θ_{1S}: nominal lateral and longitudinal cyclic angles (deg).**

Point	M_T	α_S	μ	θ_{75}	C_T/σ	θ_{1C}	θ_{1S}
$\mu = 0.3$							
6619	0.65	0.0	0.3	6.0	0.082	0.4	-4.6
8716	0.42	0.0	0.3	5.9	0.081	-0.7	-5.3
9117	0.26	0.0	0.3	5.9	0.082	-1.6	-5.7
$\mu = 0.4$							
6912	0.65	0.0	0.4	6.0	0.071	1.9	-4.5
8724	0.42	0.0	0.4	5.9	0.070	0.6	-6.3
9125	0.26	0.0	0.4	6.0	0.072	-0.6	-6.7

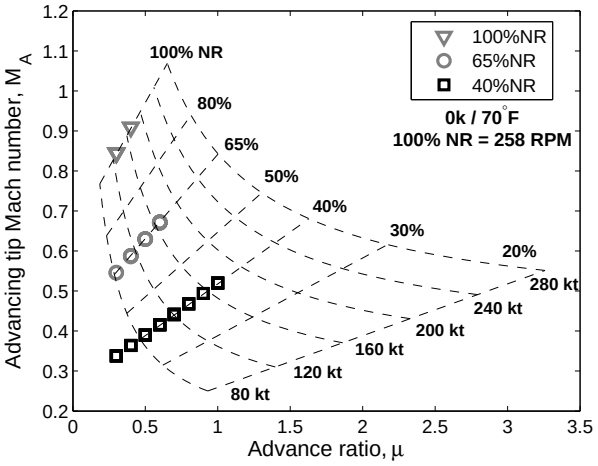

Figure 3: **Advancing tip Mach number vs. advance ratio of all slowed rotor test points.**

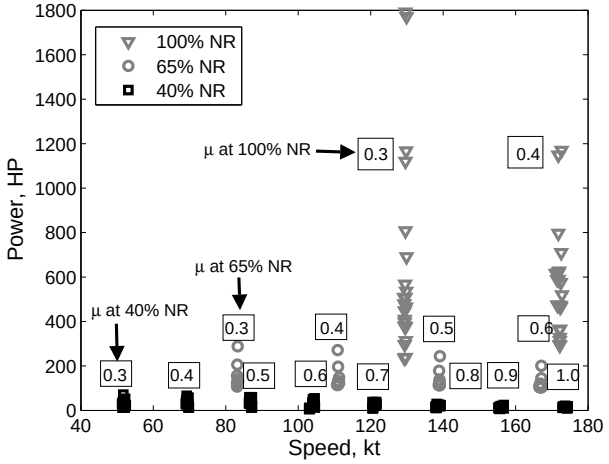

Figure 4: **Power vs. speed envelope of all slowed rotor test points.**

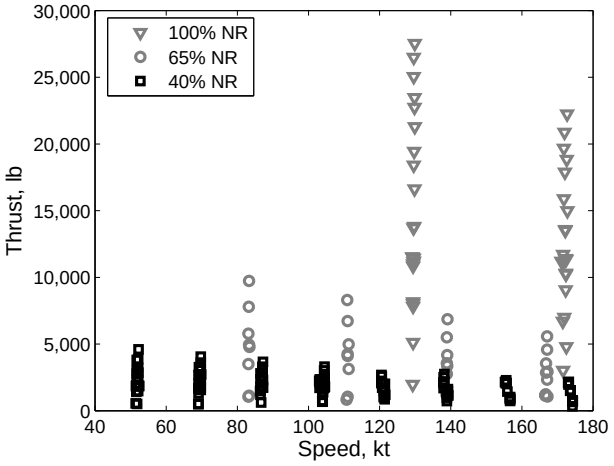

Figure 5: **Thrust vs. speed envelope of all slowed rotor test points.**

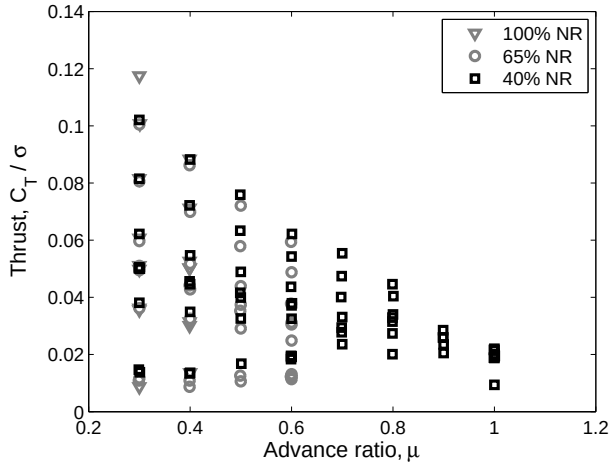

Figure 6: **Non-dimensional thrust vs. speed at** $0°$ **shaft angle.**

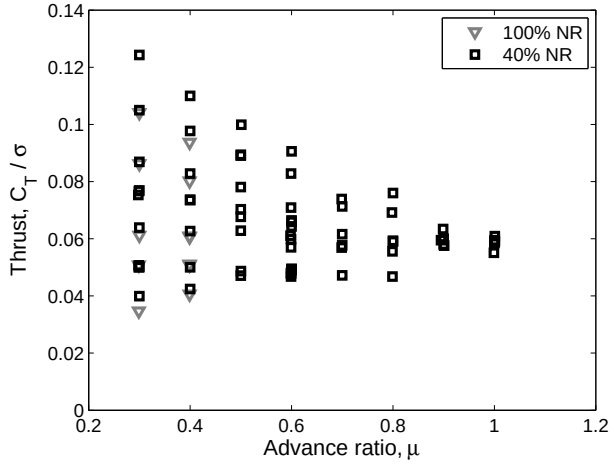

Figure 7: **Non-dimensional thrust vs. speed at** $4°$ **shaft angle (tilt back).**

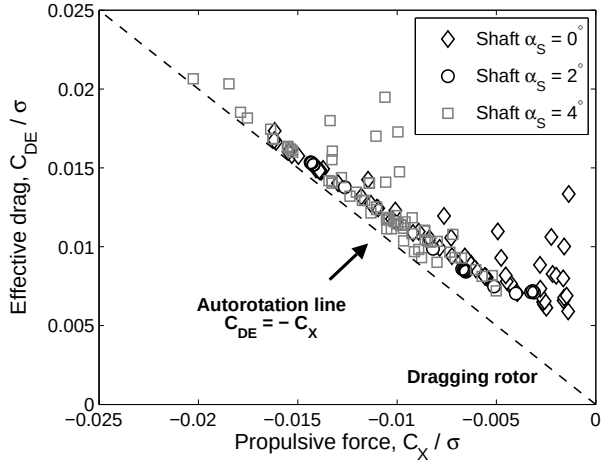

Figure 8: **Operation relative to autorotation; 40% NR.**

Table 3: **Slowed rotor test points for advance ratio (speed) sweeps at two different shaft angles.**

Point	M_T	α_S	μ	θ_{75}	C_T/σ	θ_{1C}	θ_{1S}
$\alpha_S = 0°$							
9116	0.26	0.0	0.3	4.0	0.062	-0.8	-4.2
9133	0.26	0.0	0.4	6.0	0.063	0.4	-7.4
9145	0.26	0.0	0.5	7.9	0.062	1.4	-10.0
$\alpha_S = 4°$							
9318	0.26	4.0	0.4	2.0	0.063	0.0	-4.1
9325	0.26	4.0	0.5	2.0	0.063	0.7	-4.8
9518	0.26	4.0	0.7	3.0	0.062	2.0	-6.6
9528	0.26	4.0	0.9	6.2	0.063	5.0	-10.9

Table 4: **Slowed rotor test points for thrust (collective) sweeps at two shaft angles and three advance ratios.**

Point	M_T	α_S	μ	θ_{75}	C_T/σ	θ_{1C}	θ_{1S}
$\alpha_S = 0°$							
$\mu = 0.8$;							
9155	0.26	0.0	0.8	-0.1	0.020	2.8	0.0
9156	0.26	0.0	0.8	2.0	0.033	3.3	-2.5
9157	0.26	0.0	0.8	4.0	0.034	3.9	-5.3
9158	0.26	0.0	0.8	6.0	0.040	4.3	-7.7
9159	0.26	0.0	0.8	8.0	0.045	4.4	-10.2
$\mu = 0.9$							
9162	0.26	0.0	0.9	0.0	0.021	3.6	0.3
9163	0.26	0.0	0.9	2.0	0.024	4.4	-2.3
9164	0.26	0.0	0.9	4.0	0.026	5.3	-5.2
$\mu = 1.0$							
9168	0.26	0.0	1.0	-0.1	0.019	4.7	0.8
9175	0.26	0.0	1.0	1.9	0.022	5.5	-1.8
$\alpha_S = 4°$							
$\mu = 0.8$;							
9520	0.26	4.0	0.8	-0.1	0.047	2.7	-3.1
9521	0.26	4.0	0.8	1.9	0.056	2.9	-5.5
9522	0.26	4.0	0.8	5.9	0.069	3.5	-10.5
9523	0.26	4.0	0.8	7.7	0.076	3.6	-12.6
$\mu = 0.9$							
9526	0.26	4.0	0.9	-0.1	0.058	3.6	-2.7
9527	0.26	4.0	0.9	2.0	0.060	4.4	-5.5
9528	0.26	4.0	0.9	6.2	0.063	5.0	-10.9
$\mu = 1.0$							
9531	0.26	4.0	1.0	0.0	0.061	4.5	-2.6
9530	0.26	4.0	1.0	2.0	0.059	5.6	-5.5

ROTOR PERFORMANCE

This section analyzes the measured rotor performance. The 40% NR case is studied in detail as this case extends up to $\mu = 1.0$. The 65% NR case (up to $\mu = 0.6$) and 100% NR case (up to $\mu = 0.4$) are used for comparison purposes. For all of the test points, thrust almost equals lift ($C_T \approx C_L$), but not used interchangeably to maintain consistency of nomenclature. In addition, for the case of 0° shaft angle, drag almost equals H-force ($C_D \approx C_H$).

The thrust variation with collective at 0° shaft angle at 40% NR is shown in Fig. 9. The sensitivity is reduced to almost zero at $\mu = 1.0$. The thrust variation with collective at 4° shaft angle is shown in Fig. 10. The sensitivity reverses slightly at $\mu = 1.0$. The thrust sensitivities at the two shaft angles are plotted in Fig. 11 as a function of advance ratio. Also plotted in the same figure is the thrust sensitivity to shaft angle at 0° collective. This sensitivity shows a slight increase at the lower and higher advance ratios ($\mu = 0.3$ to 0.4 and $\mu = 0.7$ to 1.0) with a dip in between, but remains nominally constant compared to the sensitivity to collective.

This thrust behavior under high advance ratios (near $\mu = 1.0$) was first reported in 1965 by Jenkins [27], and attributed to the sensitivity of longitudinal flapping (i.e. longitudinal cyclic, under trim condition) to collective being greater than its sensitivity to shaft angle. The sensitivities of the longitudinal cyclic to collective and to shaft angle, shown in Fig. 12, confirm this trend. An increase in collective makes the reverse flow regime more severe at high advance ratios, results in a progressively higher longitudinal cyclic requirement for trim, and consequently begins to offset the effect of thrust increase with collective (Fig. 11). An increase in shaft angle makes the reverse flow less severe, and because a greater reverse flow area (i.e. advance ratio) leads to a greater benefit, generally augments the effect of thrust increase with shaft angle (Fig. 11). However, an increase in collective at a higher shaft angle (4° versus 0°) appears to be detrimental to thrust beyond an advance ratio of 0.5. It is shown later that an additional mechanism which contributes significantly to the thrust behavior is the large elastic twist deformation of the blades that drives the advancing blade inboard and outboard stations to produce a differential airloading.

The power variation with thrust at 0° shaft angle is shown in Fig. 13. Each symbol represents one collective setting. Beyond $\mu = 0.7$ power reduces with increasing thrust as the rotor begins to absorb energy and generate increasingly greater propulsive force in the negative direction (drag). This is seen in Fig. 14 where the drag force is plotted versus lift. The drag sensitivity to collective increases with advance ratio, unlike thrust, and shows a steep increase beyond $\mu = 0.7$. The H-force is expected to be same as drag force at 0° shaft angle, the

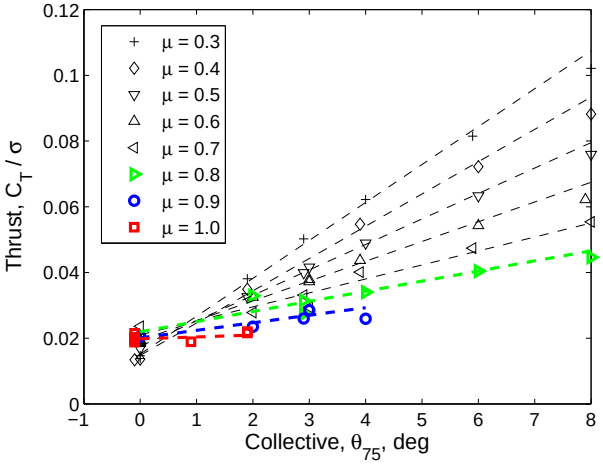

Figure 9: **Thrust vs. collective for advance ratios up to 1.0;** 0° **shaft; 40% NR.**

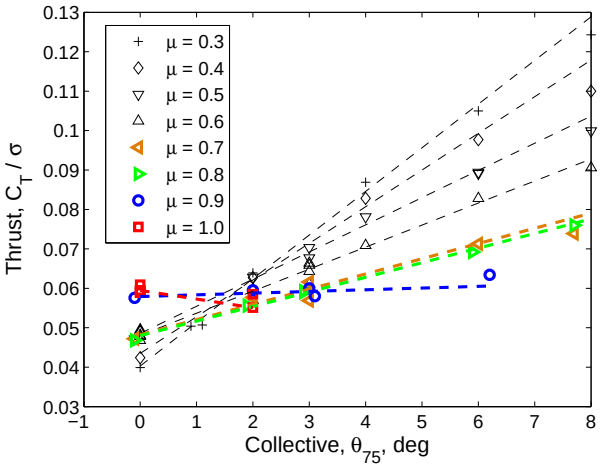

Figure 10: **Thrust vs. collective for advance ratios up to 1.0;** 4° **shaft; 40% NR.**

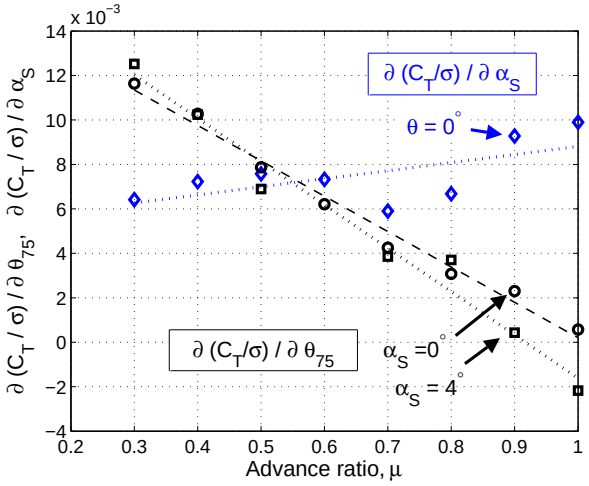

Figure 11: **Thrust sensitivity to collective at two shaft angles** (0° **and** 4°)**, and to shaft angle at** 0° **collective; 40% NR.**

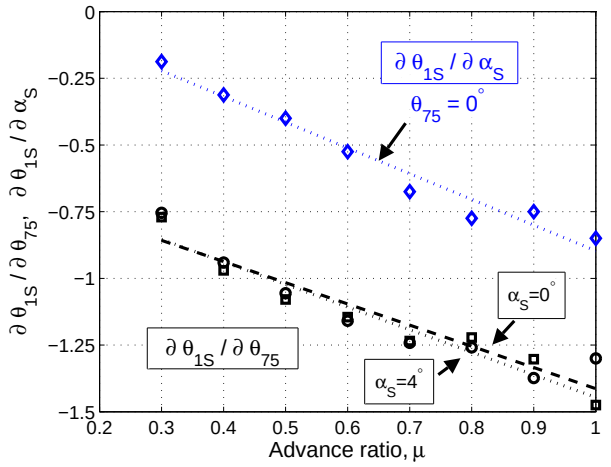

Figure 12: **Longitudinal cyclic sensitivity to collective at two shaft angles ($0°$ and $4°$), and to shaft angle at $0°$ collective; 40% NR.**

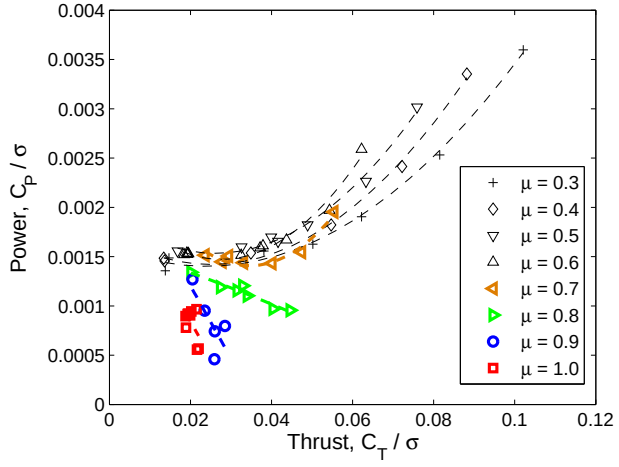

Figure 13: **Power vs. thrust for advance ratios up to 1.0; $0°$ shaft; 40% NR.**

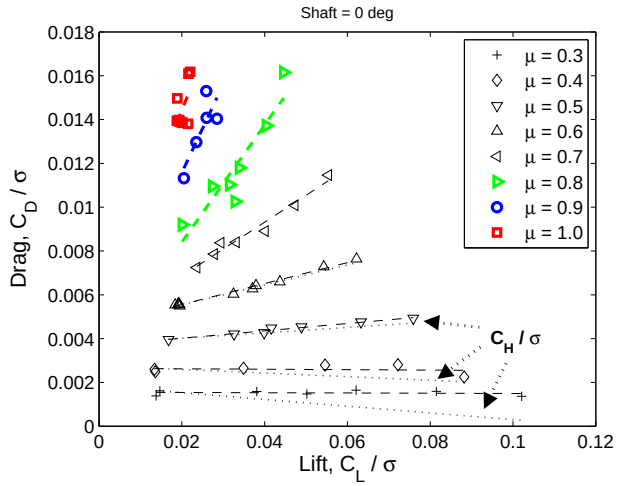

Figure 14: **Drag ($= -X \approx H$) vs. lift for advance ratios up to 1.0; $0°$ shaft; 40% NR.**

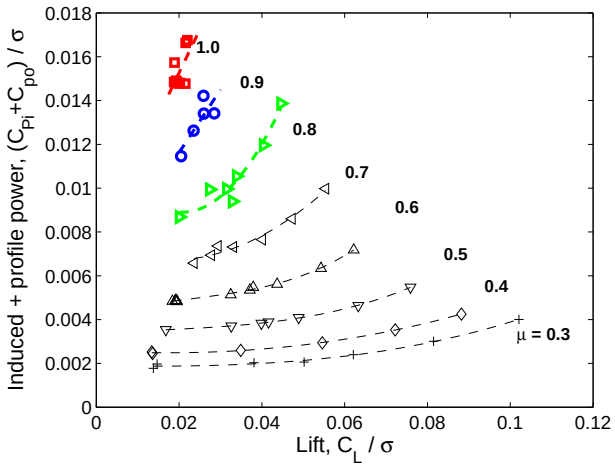

Figure 15: **Induced and profile power vs. lift for advance ratios up to 1.0; $0°$ shaft; 40% NR.**

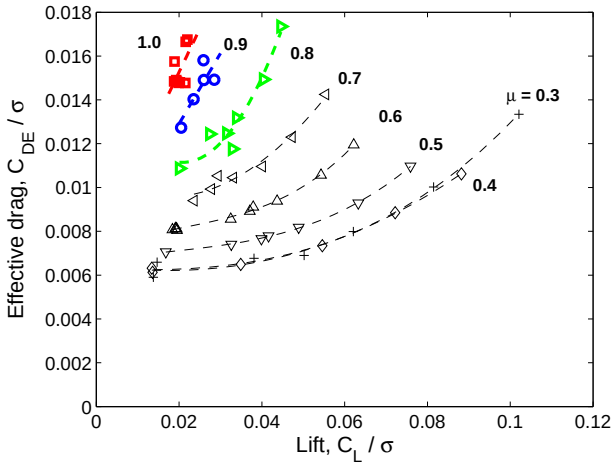

Figure 16: **Effective drag vs. lift for advance ratios up to 1.0; $0°$ shaft; 40% NR.**

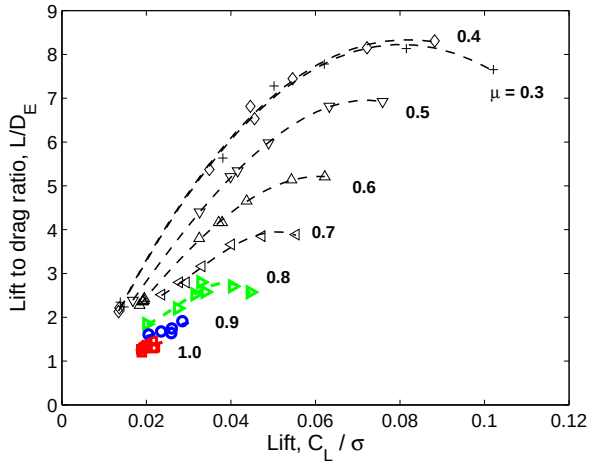

Figure 17: **Lift to drag ratio for advance ratios up to 1.0; Shaft=$0°$, 40% NR.**

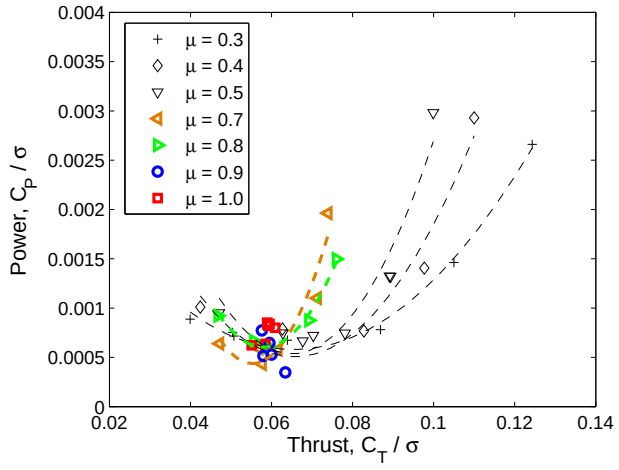

Figure 18: **Power vs. thrust for advance ratios up to 1.0; 4° shaft; 40% NR.**

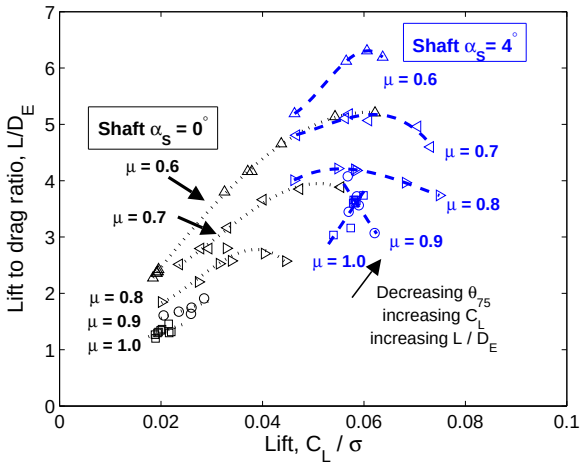

Figure 19: **Lift to drag ratio compared at zero and positive shaft angles; 40% NR.**

deviation found at the lower advance ratios and higher lift are due to the tunnel correction $\Delta\alpha$ becoming more significant (Eq. 1).

If the propulsive power (μC_X) is removed from total power (Fig. 13), then the reduction with increasing thrust at the higher advance ratios vanish and the remaining induced and profile power components ($C_{Pi} + C_{Po} = C_P - \mu C_X$), plotted in Fig. 15, show a continuous increase as expected. The effective drag (C_{DE}, where $\mu C_{DE} = C_{Pi} + C_{Po}$), shown in Fig. 16, follows the same trend, except that the lower advance ratios ($\mu = 0.3$ and 0.4) collapse to a single curve. The rotor efficiency (lift-to-drag ratio L/D_E) is shown in Fig. 17. Even though the rotor power reduces with thrust at the high advance ratios, the dragging rotor has a poor efficiency, with $L/D_E \approx 1 - 3$. At a higher shaft angle of 4° the power variation with thrust is as shown in Fig. 18. The curves show a more distinct optimum (around $C_T/\sigma = 0.06$) compared to the 0° shaft angle case (Fig. 13). The L/D_E values at the two shaft angles are compared in Fig. 19 for the high advance ratios. A positive shaft angle increasing efficiency is typical of rotors, what is different for the slowed rotor, is that the efficiency is maximized by a decrease in collective when operating beyond thrust reversal. This is the case for $\mu = 1.0$ at $\alpha_S = 4°$ in Fig. 19.

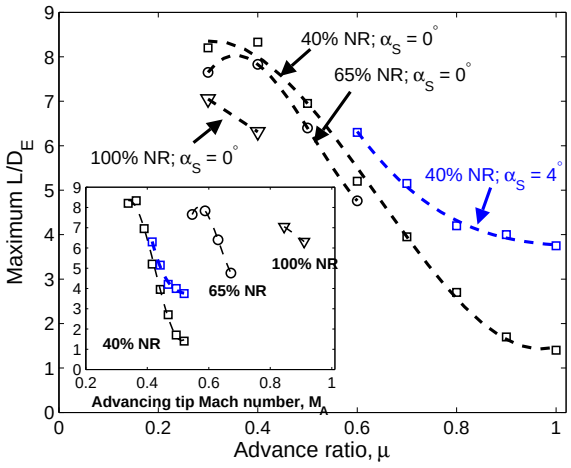

Figure 20: **Maximum lift to drag ratios.**

The maximum efficiencies are plotted in Fig. 20. At any given advance ratio, i.e. a given reverse flow area, the maximum is higher for the slowed rotor. This is most likely the result of lower profile drag at a lower tip speed. The reduction with advance ratio is clearly a function of reverse flow alone as the advancing tip Mach numbers appear far from drag divergence (see subplot). However, it is shown later in the section on pressures and airloads that for the high advance ratios, large swaths of supersonic flow exist on the lower surface of the advancing side. Thus, even though the advancing tip Mach number is low, high wave drag penalty from local supersonic flow is a significant contributor to the reduction shown in Fig. 20.

The increase in rotor efficiency with a positive shaft angle is produced at the cost of an increase in drag, which implies an increase in propulsive power required from auxiliary sources and hence a decrease in vehicle efficiency. This trade-off is illustrated in Fig. 21. Here, the rotor power is re-plotted versus its propulsive force multiplied by speed. The latter is the power for propulsion: available, if propulsive force is positive (propelling rotor), or required, if propulsive force is negative (dragging rotor). This power is represented by the straight line $C_P = \mu C_X$ in the plot. The test data correspond to the collective angle sweeps carried out at each advance ratio. At the lower advance ratios (up to $\mu = 0.7$ for $\alpha_S = 0°$ and up to $\mu = 0.8$ for $\alpha_S = 4°$) an increase in collective increases both propulsive power and rotor power. At the higher advance ratios, an in-

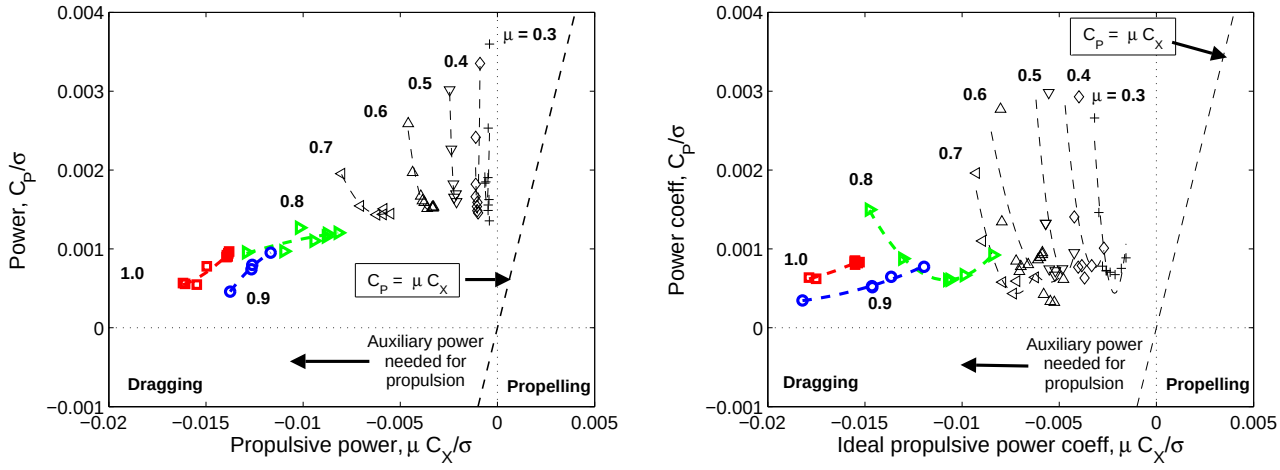

(a) Shaft angle $\alpha_S = 0°$

(b) Shaft angle $\alpha_S = 4°$

Figure 21: **Total power vs. propulsive power showing auxiliary power needed to overcome drag at shaft angles** $0°$ **and** $4°$**; 40% NR.**

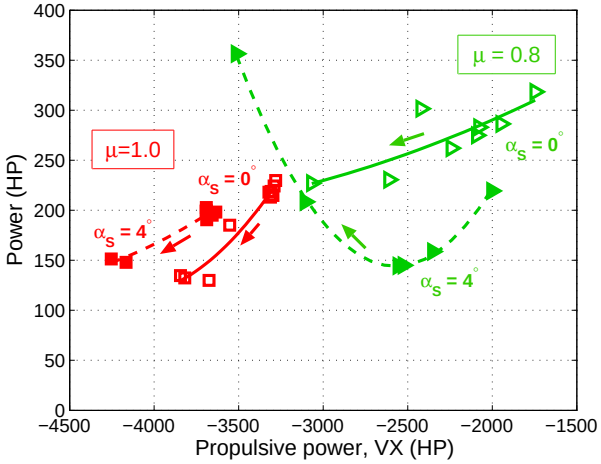

Figure 22: **Total power vs. propulsive power (HP) for advance ratios** $\mu = 0.8$ **(green),** 0.9 **(blue) and** 1.0 **(red) at shaft angles** $0°$ **(open symbols) and** $4°$ **(solid symbols); arrows mark direction of increasing collective.**

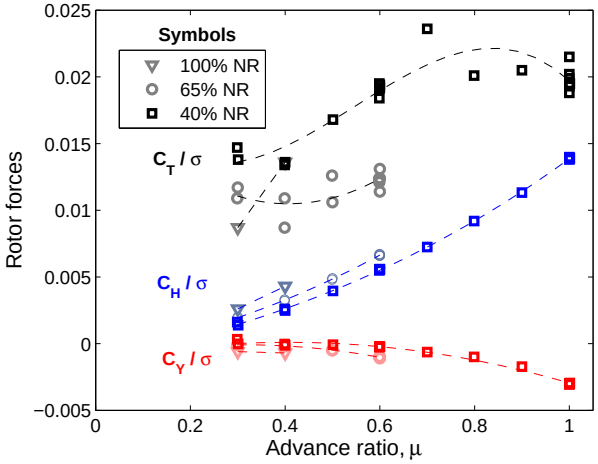

Figure 23: **Rotor forces at** $0°$ **shaft and** $0°$ **collective; Conventional vs. slowed RPM.**

crease in collective decreases rotor power but increases propulsive power. A comparison of Figs. 21(a) and 21(b) shows that for operations at the highest advance ratios ($\mu = 0.9$ and $\mu = 1.0$), a shaft angle of $\alpha_S = 0°$, even though inefficient for the rotor alone (Fig. 19), appears more suitable as it requires significantly less propulsive power. The trade-off is more clearly illustrated in Fig. 22 where the curves corresponding to $\mu = 0.8$ and 1.0 are re-drawn at the two shaft angles in terms of dimensional power (HP). It shows, at $\mu = 0.8$, increasing shaft angle at the lowest collective, increases propulsive power and decreases rotor power by comparable amounts. Thus the higher shaft angle – with better rotor efficiency (greater L/D_E) – is the preferred mode of operation. But at $\mu = 1.0$, where the increase in propulsive power and decrease in rotor power are +400 HP and -25 HP respectively, the lower shaft angle – with worse rotor efficiency – is the preferred mode of operation. The price to pay for carrying an inefficient rotor is a loss in lift that must be compensated for by other means.

From considerations of propulsive power, minimum collective operations are of interest at high advance ratios. The rotor forces from a nominally zero collective angle sweep is shown in Fig. 23. The sweep also represents the closest approach to a zero thrust sweep – useful for analyses validation of profile components. Because of the high built-in twist, the thrust produced is still non-zero, but the rotor forces are near-

est to their profile contributions (C_{Ho} and C_{Yo}).

In summary, the performance measurements were consistent with previous test data. A drop off in thrust sensitivity to collective at high advance ratios, along with a reversal at 1.0, was observed as expected. A dramatic drop off in efficiency was observed at the high advance ratios. The efficiency was higher at a positive shaft angle but at the expense of greater drag.

BLADE LOADS AND HUB LOADS

In this section, the blade structural loads and hub loads are compared between the nominal and slowed rotors. As before, the 40% NR case is studied in detail, the others used for comparison. The oscillatory (1P and higher) and vibratory (3P and higher) harmonics of blade loads and first blade passage (4P) hub loads are considered. The steady loads are ignored.

The structural loads are examined in dimensional form, as these are directly relevant to blade design. The parametric comparison of flight conditions and break down into harmonics are still carried out in non-dimensional form. That is, thrust variation is in terms of C_T/σ, speed in terms of μ, and harmonic content relative to operating RPM (/rev, P). This is appropriate because these non-dimensional parameters are direct indicators of proximity to stall, extent of reverse flow, and blade dynamic response. For purposes of plotting, every other azimuthal data is plotted (128 points per rev). Flap bending is positive for upper surface in compression, chord bending is positive for trailing edge in compression, and torsion moment is positive for nose-up. Pitch link load is positive in extension (nose-up).

The rotor frequencies, shown in Table 5, are very different for the slowed rotor beyond the third mode. Even though the rotor is generally stiffer (relative to its reduced rotational frequency), the second flap frequency still lies near 3/rev and remains the dominant driver of blade loads. A notable difference at 40%NR is the large frequency gap between the second flap and first torsion modes. The absence of any mode near 5/rev has important ramifications on vibratory hub loads, as shown later.

Table 5: **Predicted slowed rotor frequencies compared to nominal.**

100%NR /rev	65%NR /rev	40%NR /rev	Mode
0.276	0.287	0.318	Lag
1.037	1.040	1.048	Flap
2.83	2.98	3.33	Flap
4.39	5.66	7.33	Torsion
4.69	6.70	10.54	Lag

Consider as the baseline, the flap bending moments on the nominal rotor (100%NR) in a high speed con-

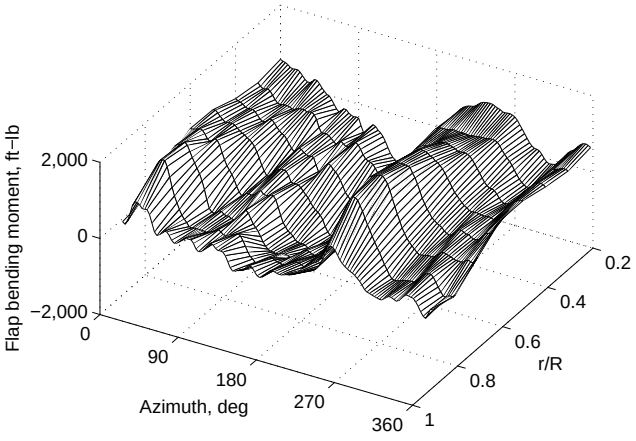

Figure 24: **Flap bending moment at 100% NR;** $\mu = 0.4$**,** $C_T/\sigma = 0.07$ **(T=15885 lb),** $\alpha_S = 0°$**.**

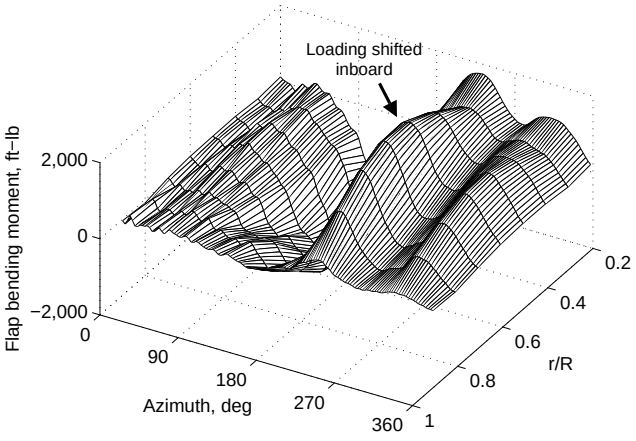

Figure 25: **Flap bending moment at 40% NR;** $\mu = 0.9$**,** $C_T/\sigma = 0.063$ **(T=2280 lb),** $\alpha_S = 4°$**.**

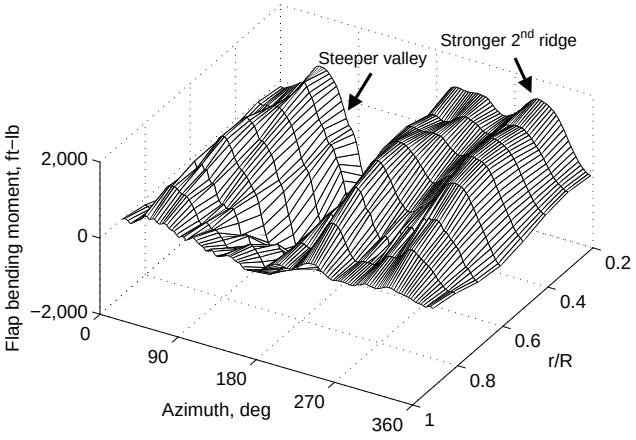

Figure 26: **Flap bending moment at 40% NR;** $\mu = 1.0$**,** $C_T/\sigma = 0.022$ **(T=780 lb),** $\alpha_S = 0°$**.**

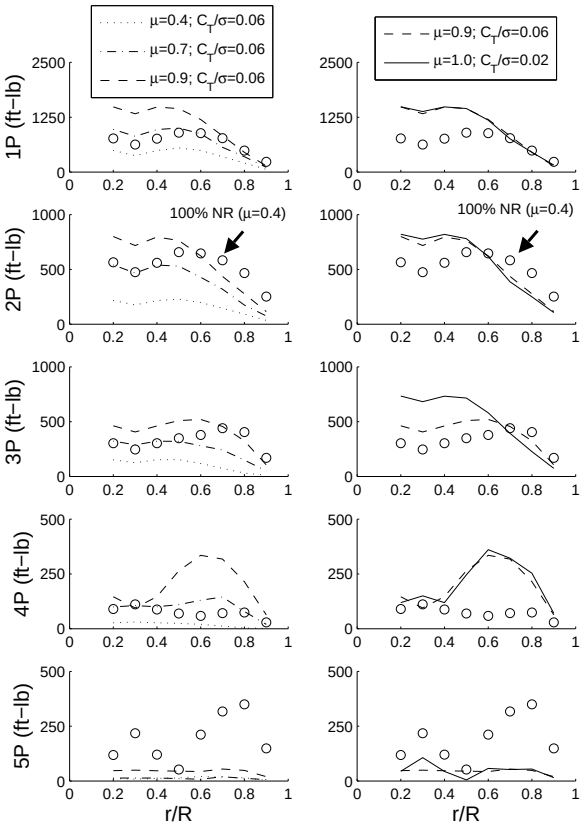

Figure 27: **Flap bending moment harmonics for nominal and 40% NR slowed rotor; nominal: $\mu = 0.4$, $C_T/\sigma = 0.07$, $\alpha_S = 0°$ (shown as symbols-○); slowed: $\mu = 0.4$–0.9, $C_T/\sigma = 0.06$, $\alpha_S = 4°$ and $\mu = 1.0$, $C_T/\sigma = 0.02$, $\alpha_S = 0°$ (shown as lines).**

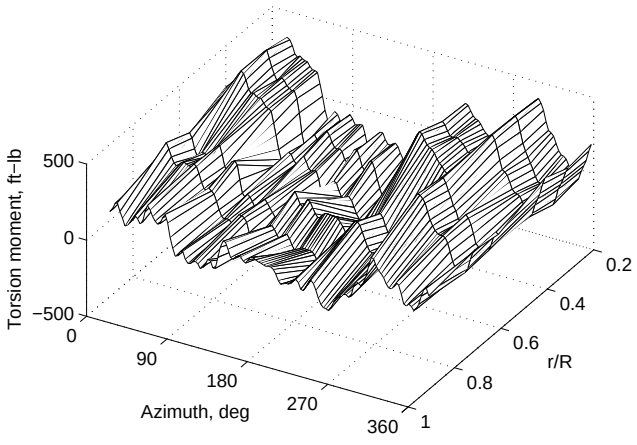

Figure 28: **Torsion moment at 100% NR; $\mu = 0.4$, $C_T/\sigma = 0.07$, $\alpha_S = 0°$.**

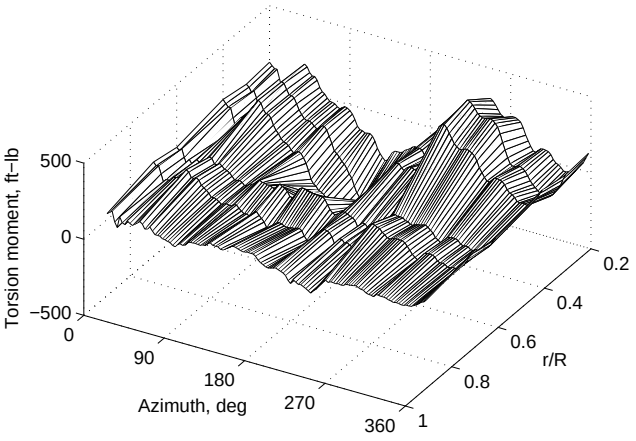

Figure 29: **Torsion moment at 40% NR; $\mu = 0.9$, $C_T/\sigma = 0.063$, $\alpha_S = 4°$.**

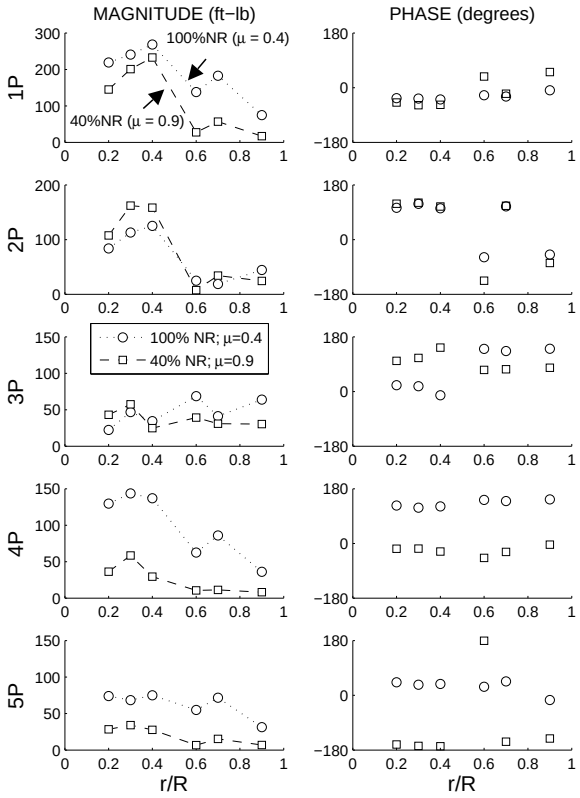

Figure 30: **Torsion moment harmonics for nominal and 40% NR slowed rotor; nominal: $\mu = 0.4$, $C_T/\sigma = 0.07$, $\alpha_S = 0°$; slowed: $\mu = 0.9$, $C_T/\sigma = 0.06$, $\alpha_S = 4°$.**

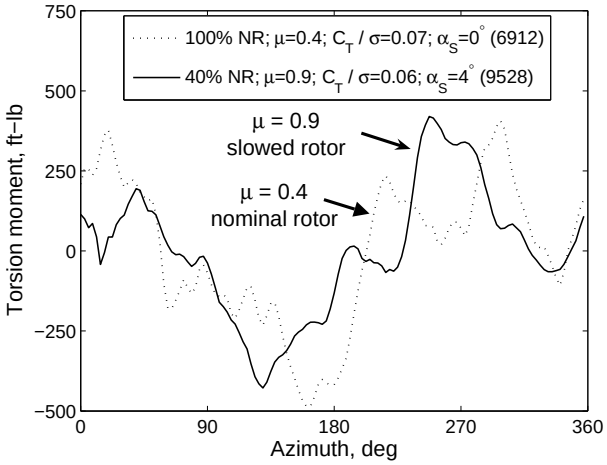

Figure 31: **Torsion moment at 30% R for nominal and 40% NR slowed rotor; nominal:** $\mu = 0.4$, $C_T/\sigma = 0.07$, $\alpha_S = 0°$; **slowed:** $\mu = 0.9$, $C_T/\sigma = 0.06$, $\alpha_S = 4°$.

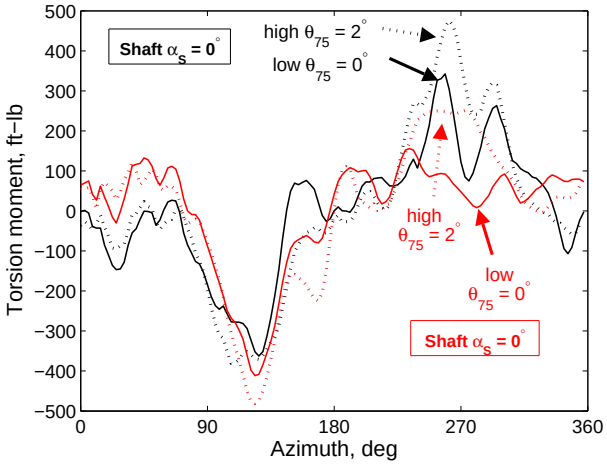

Figure 32: **Study of retreating side impulse in torsion moment (30% R) at $\mu = 1.0$ for a 40% NR slowed rotor showing increased severity at lower shaft angle and higher collective.**

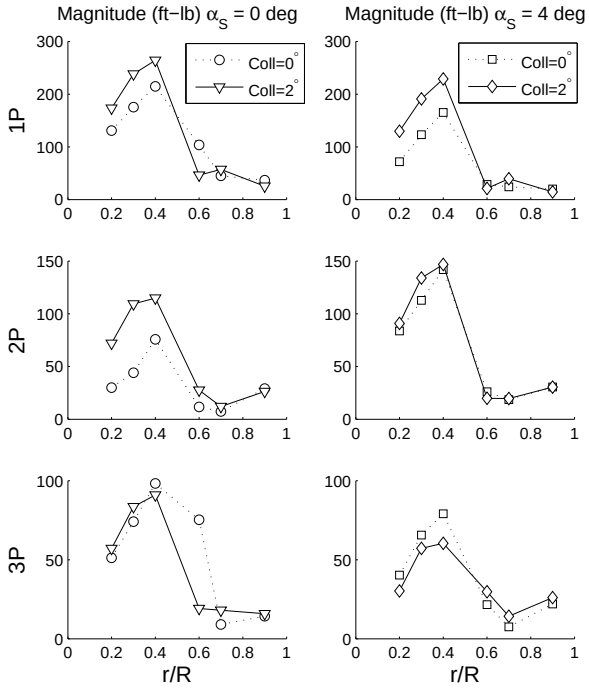

Figure 33: **Effect of collective increase on 1-3/rev torsion moments at $\mu = 1.0$ for two different shaft angles; $\alpha_S = 0°$ (θ_{75}=0° and 2° produces $C_T/\sigma = 0.019$ and 0.022) and $\alpha_S = 4°$ (θ_{75}=0° and 2° produces $C_T/\sigma = 0.061$ and 0.059 − reversal); 40% NR.**

dition: $\mu = 0.4$, $C_T/\sigma = 0.071$ and $\alpha_S = 0°$, Point 6912 (P6912) in Table 2. The azimuthal variations of the oscillatory bending moments are plotted for all radial stations from the root to the tip (20%–90%R) in a 3-dimensional plot in Fig. 24. If RPM is swept down to 40%NR keeping advance ratio constant, along the points in Table 2, the peak-to-peak bending moments reduce by about 50% (not shown). But as advance ratio increases, with RPM constant at 40% NR, the bending moments build up again, eventually reaching the baseline level and then higher. To study the variation with advance ratio, consider the sweep at $\alpha_S = 4°$ in Table 3. The thrust level is closest to the baseline. The bending moments at the end of this sweep, at $\mu = 0.9$, are shown in Fig. 25. Even though the thrust level is lower than the baseline, the moments are higher. The loading pattern is also qualitatively different. The second mode is still dominant but the peak loading is now shifted inboard. The bending moments at $\mu = 1.0$, shown in Fig. 26, corresponding to a point with an even lower thrust level of $C_T/\sigma = 0.022$ (P9175, Table 4), show even greater magnitudes. The advancing side drop is steeper and the fourth quadrant oscillation stronger. Note that the dimensional thrusts for both the high advance ratio points are very low, 2,280 lb and 780 lb, compared to a thrust of 15,885 lb for the baseline.

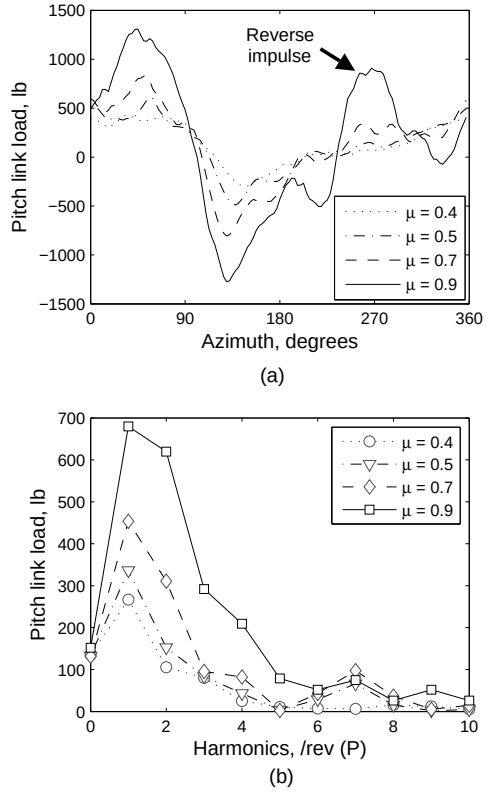

Figure 34: **Pitch link load variation with advance ratio;** $\mu = 0.4 - 0.9$**,** $C_T/\sigma \approx 0.06$**,** $\alpha_S = 4°$**; 40% NR.**

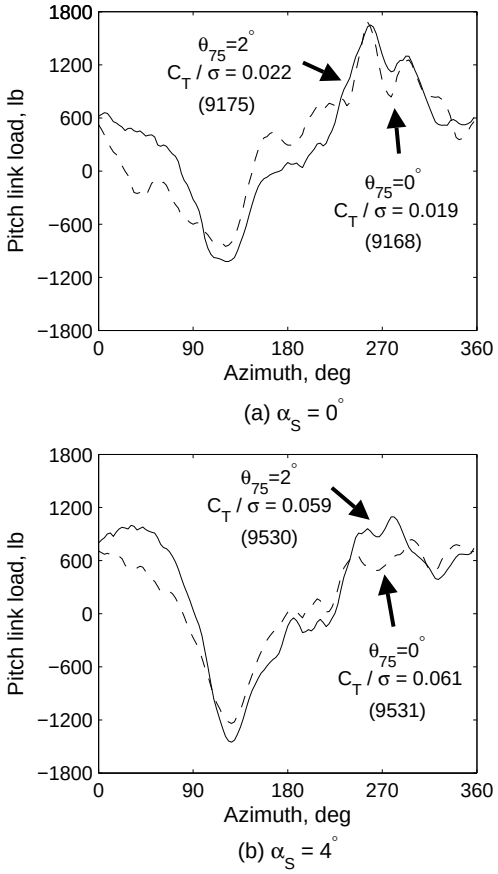

Figure 35: **Effect of collective on pitch link load at** $\mu = 1.0$ **for two different shaft angles;** $\alpha_S = 0°$ **(**θ_{75}**=0° and 2° produces** $C_T/\sigma = 0.019$ **and** 0.022**) and** $\alpha_S = 4°$ **(**θ_{75}**=0° and 2° produces** $C_T/\sigma = 0.061$ **and** 0.059 **− reversal); 40% NR.**

The bending moment harmonics are shown in Fig. 27. The left hand side column of plots shows the variation with increasing advance ratio at the same thrust level. The right hand side column of plots compares two highest advance ratio cases at high and low thrust levels. The baseline is plotted in both for comparison. The left hand side plots show that the 5P harmonic is negligible for the slowed rotor, regardless of advance ratio. The 4P harmonic increases dramatically beyond $\mu = 0.7$. The 3P harmonic behaves similarly as the baseline and has a comparable magnitude. The 1P and 2P harmonics, which determine the peak-to-peak variation, are 50-100% higher than baseline inboard of 70% R at the highest advance ratio. The right hand side plots indicate that this loading pattern is independent of thrust – remains the same regardless of $C_T/\sigma = 0.06$ or 0.02. The 3P harmonic in fact increases with a decrease in thrust. Even though these comparisons are not consistent parametric variations (the baseline has a higher thrust and a lower shaft angle, and the $\mu = 1.0$ slowed rotor point has a different shaft angle from the other slowed rotor points) they illustrate the fact that the slowed rotor operating at a lower non-dimensional thrust and negligible dimensional thrust carries bending moments higher than the highest levels of the nominal rotor under high speed conditions. The net thrust level is not even a remote indicator of these load levels.

A possible reason behind the high loads is a higher than usual differential airloading between the inboard and outboard sections of the advancing side. If the reverse flow produces little or no lift on the retreating side, this differential airloading is required to trim the rotor. If the reverse flow produces negative lift, then the differential airloading may even be greater, with the outboard stations required to generate negative lift. These conjectures are tested in the next section on pressures and airloads, but the implication here is that the elastic twist on the blades must be significantly high to produce this differential airloading. An examination of the torsion moments indicate that this may indeed be true.

The torsion moment for the nominal rotor is shown in Fig. 28. The torsion moment for the slowed rotor at $\mu = 0.9$ and at a comparable thrust level is shown in Fig. 29. The peak-to-peak magnitudes are again simi-

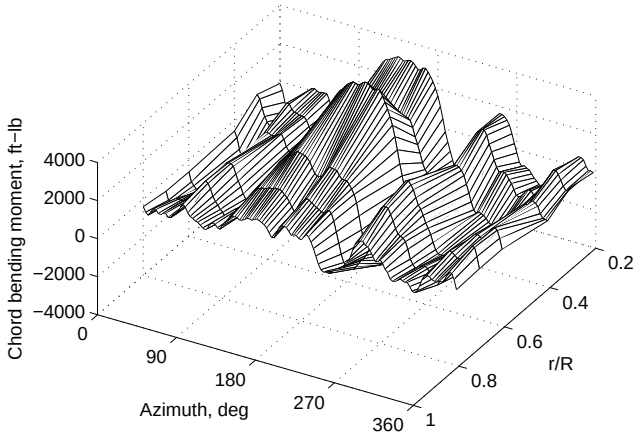

Figure 36: **Chord bending moment at 100% NR; $\mu = 0.4$, $C_T/\sigma = 0.07$, $\alpha_S = 0°$.**

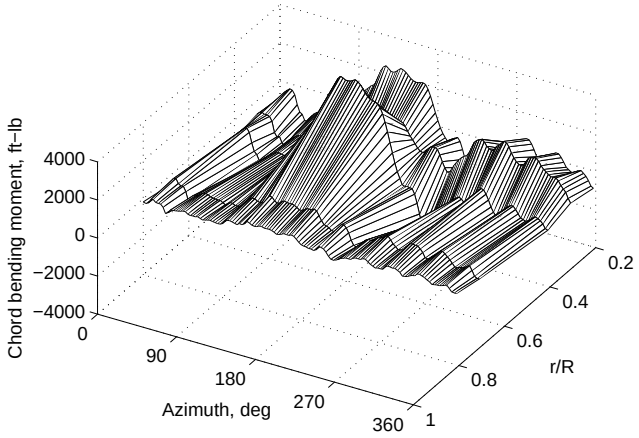

Figure 37: **Chord bending moment at 40% NR; $\mu = 0.9$, $C_T/\sigma = 0.063$, $\alpha_S = 4°$.**

lar. The spanwise distribution of harmonics, shown in Fig. 30, indicates a large 1P gradient between the inboard and outboard stations (between 40% and 60% R) for the slowed rotor. The phase angle remains the same. The 2P harmonic also shows about a 20% increase at the inboard stations. The vibratory harmonics are in general lower than the nominal rotor, except for the 3P harmonic, which has a comparable magnitude.

The azimuthal variation of torsion moment at 30% R are compared in Fig. 31. In the high advance ratio case, the peak loading is more clearly determined by the waveform in the retreating side. It is shown later, that the increase in loading around 240° azimuth is a direct consequence of the reverse flow negative lift shifting aft towards 3/4-c (1/4-c chord of reverse airfoil) and producing a nose up pitching moment impulse. Note that the nominal rotor also shows an impulsive behavior in the fourth quadrant – around 300° – but this behavior arises out of a 4/rev response and is phenomenologically different. The increase in torsion loading on the retreating side due to reverse flow was first reported in 1969 by Niebanck [37] (on a 9 ft dia model rotor at $\mu = 1.47$, $\alpha_S = 0°$, and $\theta_{75} = 2°$) and the loading pattern observed here is similar.

The retreating side torsion loading is examined in more detail in Fig. 32. The figure contains two pairs of plots, one pair each for shaft angles of 0° and 4°. For each shaft angle, two collective angles of 0° and 2° are considered. These correspond to the collective sweeps at $\mu = 1.0$ in Table 4. The retreating side impulse increases with collective angle due to increase in reverse flow angle of attack. It diminishes with shaft angle due to decrease in reverse flow angle of attack. The reverse flow is clearly less severe for a positive shaft angle.

Note however, that it was the positive shaft angle that produced a thrust reversal at $\mu = 1.0$, between 0° and 2° collectives (Table 4 and Fig. 10). A possible explanation of this apparent inconsistency is related to elastic twist at high advance ratios. The increasingly higher (negative) longitudinal cyclic needed to trim the rotor, due to the little (or negative) lift on the retreating side, drives the advancing side lower surface into super-critical flow and the resulting high pitching moments generate large elastic twist. On the one hand, this twist drives the outboard sections deeper into negative lift. On the other hand, it allows the inboard sections to produce more lift. The more severe the reverse flow (i.e. more negative the reverse flow lift), the more severe the twist and greater the contributions of inboard and outboard twists to positive and negative lift. A harmonic break down of torsion moments (Fig. 33) suggests that the effect of increase in collective influences the inboard twist more. Thus, a lower shaft angle with more severe reverse flow can show a delay in thrust reversal compared to the higher shaft angle. However, because the reversals obtained in this test are weak with thrust differences of only $\Delta C_T/\sigma \approx 0.002$, this conjecture cannot be tested conclusively. Some of its implications, however, are tested in the next section where it is shown that the advancing side is indeed immersed deeply into negative lift and the lower surface indeed contains large regions of supersonic flow.

The pitch link loads behavior is similar to the inboard torsion moment, as expected. Figures 34 and 35 summarize its behavior for an advance ratio sweep, and thrust and shaft angle sweeps at the highest advance ratio, respectively. The pitch link loads are consistent with the torsion moments shown earlier in Figs. 31 and 32. One difference is that the peak-to-peak torsion moment is determined by the retreating side impulse $\mu = 0.9$ onwards (see Fig. 31), whereas the pitch link load peak is not (see Fig. 34), and begins to be determined by the impulse only $\mu = 1.0$ onwards (Fig. 35(a)). However, once it appears, the impulse is a key source of vibratory harmonics. As shown in

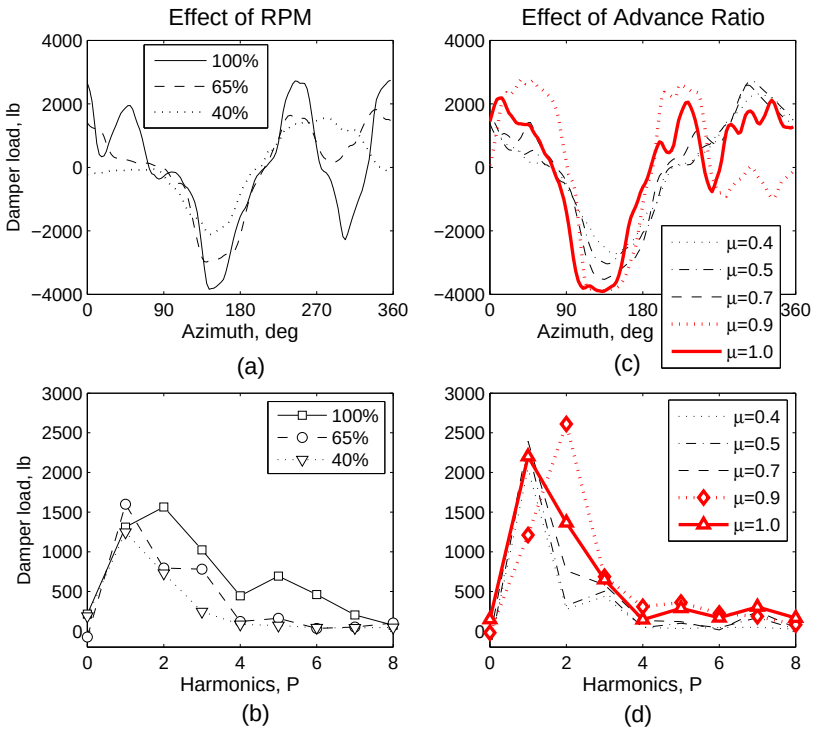

Figure 38: **Effect of RPM and advance ratio variation on damper loads; (a) and (b):** $\mu = 0.4$, $C_T/\sigma = 0.07$, $\alpha_S = 0°$**; (c) and (d):** $C_T/\sigma \approx 0.06$, $\alpha_S = 4°$**; 40% NR.**

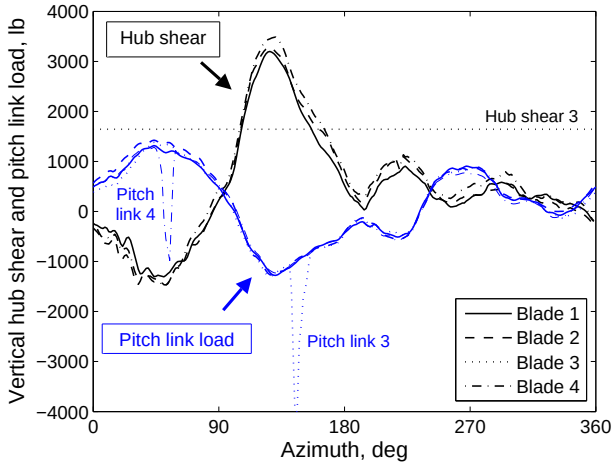

Figure 39: **Vertical hub shear and pitch link loads on four blades;** $\mu = 0.9, C_T/\sigma = 0.063, \alpha_S = 4°$**; 40% NR.**

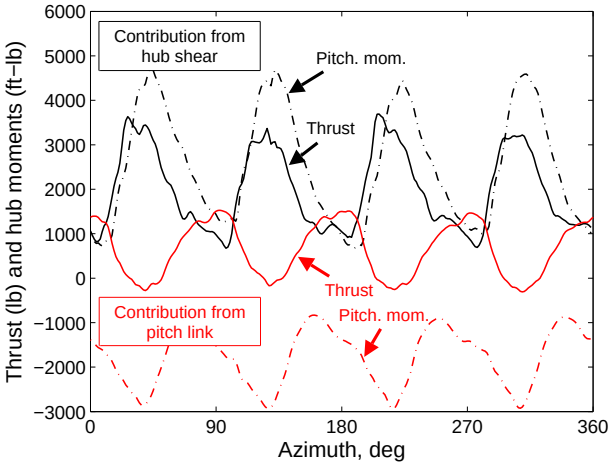

Figure 40: **Contribution of hub shear and pitch link loads on hub loads;** $\mu = 0.9, C_T/\sigma = 0.063, \alpha_S = 4°$**; 40% NR.**

Fig. 34(b), the sudden increase in 3-5P content beyond $\mu = 0.7$ is a direct consequence of the impulse.

The chord bending moment for the nominal rotor is shown in Fig. 36. The chord bending moment for the slowed rotor at $\mu = 0.9$ at a comparable thrust level is shown in Fig. 37. The 50% and 60%R gages were dysfunctional for the slowed rotor. The outboard moments, at 70% and 80%R, are benign. The inboard moments, 20%–40%R, are primarily determined by damper load similar to the nominal rotor. The damper load is studied in Fig. 38. With reduction in RPM, the load is reduced, Fig. 38(a). The 1P load remains the same but the 2P and higher loads decrease, Fig. 38(b). This implies there is little motion at these frequencies to contribute to any substantial loss in damping available at the lag frequency. Thus, lag in-

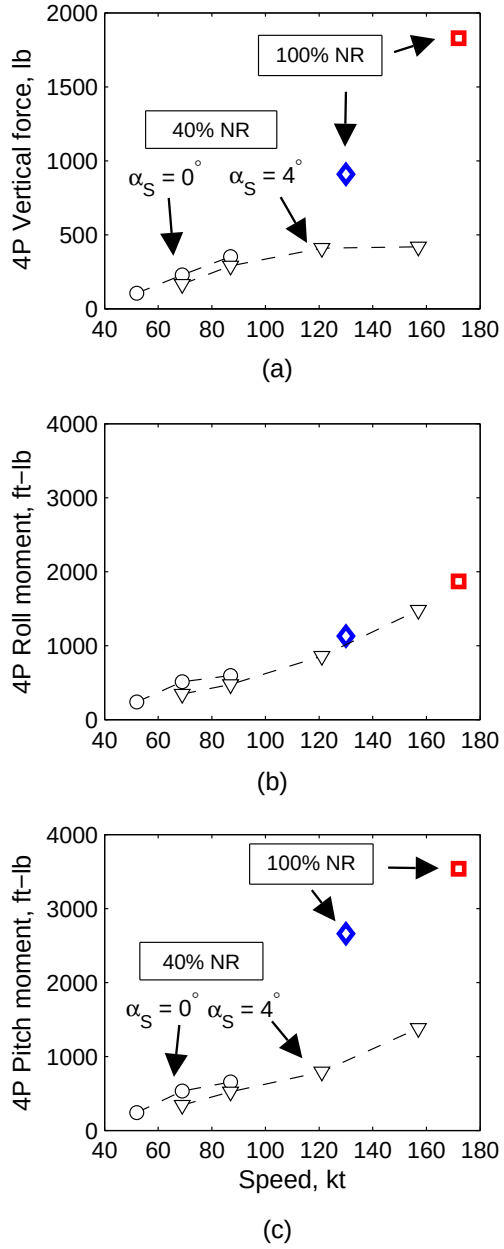

Figure 41: **Vibratory hub loads vs. speed for nominal and 40% NR slowed rotors; nominal:** $\mu = 0.3, C_T/\sigma = 0.082, \alpha_S = 0^\circ$ **(P6619) (symbol-**$\Diamond$**);** $\mu = 0.4, C_T/\sigma = 0.071, \alpha_S = 0^\circ$**, (P6912) (symbol-**$\square$**); slowed: speed sweep at** $C_T/\sigma = 0.06, \alpha_S = 0^\circ$ **(symbol-**$\circ$**) and at** $C_T/\sigma = 0.06, \alpha_S = 4^\circ$ **(symbol-**$\triangledown$**).**

stability was not a concern during the tests. Increasing advance ratio increases the loads back up to nominal levels at $\mu = 1.0$, Fig. 38(c). There is a curious 2P spike around $\mu = 0.9$ the reasons behind which are not understood, Fig. 38(d).

The effect of advance ratio on oscillatory hub loads is evaluated using data from the rotating vertical hub shears and pitch link loads. These measurements are combined to provide estimates for the vertical force and moments at the hub. purpose. Gage failures are compensated for with phase shifted data from functional gages. For example, Fig. 39 shows the hub shears and pitch link loads in one of the high advance ratio flights. Because the measurements are repeatable (within 2–5%), the faulty gages (on hub arm of blade 3 and pitch links of blades 3 and 4) are replaced with data from blade 1. The contributions from hub shear and pitch link loads are both important, particularly when the pitch link loads are high. For example, Fig. 40 shows the the contributions separately for the same flight. Note that, ideally, the rotor balance would be used to provide estimates for the oscillatory hub loads. However, it is known that the transfer function between balance readings and hub loads changes significantly between 4P frequency at 100% NR (17.2 Hz) and 4P frequency at 40% NR (6.9 Hz). A dynamic calibration of the balance that accounts for this change is currently under study.

The 4P hub loads are shown in Fig. 41 as a function of RPM and tunnel speed. Unlike the blade loads, the hub loads appear to be relatively benign for the slowed rotor. The two nominal points correspond to the $\mu = 0.3$ and 0.4 points in Table. 2. These are compared to the slowed rotor points for the two speed sweeps given in Table. 3 – the same conditions for which blade loads were analyzed earlier. The 4P vertical force is at least 50% lower for the slowed rotor. Even though the flap bending moments showed a dramatic increase in 4P harmonic (Fig. 27), the increase mostly occurred outboard of 40% R and did not affect the shear loading inboard. The rolling moment is already low, and remains comparable between the nominal and slowed rotors. The pitching moment is reduced by more than 50%. The reason behind the pitching moment reduction is the vanishing of the 5P harmonic from the flap bending moments (Fig. 27). The same trend was also observed in the chord bending moments (not shown). The vanishing 5P is the result of the large frequency gap between the second flap and first torsion modes as shown earlier in Table 5.

In summary, the blade loads on the slowed rotor are comparable to or higher than the nominal rotor beyond an advance ratio of $\mu = 0.8$. Yet, the vibratory hub loads remain benign with at least 50% reduction in vertical force and pitching moments. The blade loads appear to be driven by a high differential airloading between the inboard and outboard sections of the blade

potentially caused by a large elastic twist deformation. The reduction in hub loads is due partly to the frequency gap between second flap and first torsion modes leading to the vanishing of 5P blade loads. At advance ratios beyond 0.9, the peak torsion loads were determined (or significantly affected) by a nose up impulsive loading on the retreating side.

BLADE PRESSURES AND AIRLOADS

This section analyses the azimuthal and chordwise variations of blade surface pressures and sectional airloads.

The radial stations where enough pressure taps remained functional for sectional airloads calculation were 22.5%, 86.5%, 92%R, and 99% R. Most of the inboard sections that are important for reverse flow, 40% to 77.5% R, all suffered losses. Nevertheless, many of the taps remained functional in these stations, and a study of these functional taps provide significant insights into the flow phenomena in this regime. These phenomena can then be associated with the performance and structural load patterns observed in the previous sections.

The azimuthal variation of pressures are studied as offset plots of $-M^2C_p$, where M is the local incident Mach number and C_p the pressure coefficient. In these plots, only the leading-edge (or nearest working tap) values are correct, the rest are arbitrarily offset to reveal chordwise and azimuthal trends. Because negative pressure is plotted, an increase implies flow acceleration, hence suction. For accelerated flow, the onset of local supersonic flow is estimated by the 1-D steady isentropic relation:

$$C_p = \frac{2}{\gamma M^2}\left[\left(\frac{1+\frac{\gamma-1}{2}M_l^2}{1+\frac{\gamma-1}{2}M^2}\right)^{\frac{\gamma}{1-\gamma}} - 1\right] \qquad (8)$$

where M_l is the local surface Mach number. Substituting $M_l = 1$ and M at any azimuth provides an estimate $C_P = C_P^*$ of the surface pressure for onset of supersonic flow.

Consider one of the severest reverse flow points (highest advance ratio, highest collective, zero shaft angle): $\mu = 1.0$, $\theta_{75} = 1.9°$, and $\alpha_S = 0°$ (P9175). The upper and lower surface pressures at 22.5%R are shown in Figs. 42 and 43 respectively. The azimuthal extent of reverse flow is demarcated in the plots by vertical lines. There is suction on both surfaces in the reverse flow region but on the lower surface it appears to increase in strength from leading-edge (LE) towards trailing-edge (TE). If the TE were to behave as the effective LE of the reversed airfoil it is expected to operate under greater suction. Unfortunately the three taps between 0.395c to TE are dysfunctional and therefore whether the strength of these suction peaks indeed increase towards the TE cannot be ascertained.

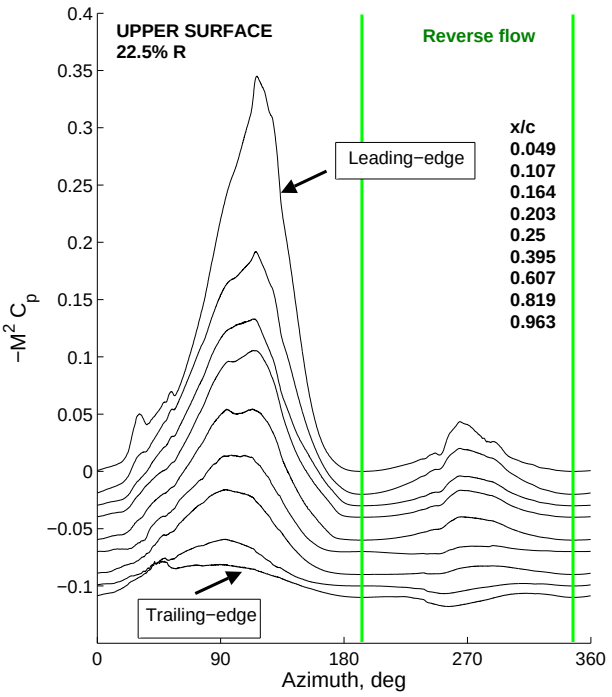

Figure 42: **Upper surface pressures at 22.5% R; $\mu = 1.0$; $C_T/\sigma = 0.022$ ($\theta_{75} = 2°$), $\alpha_S = 0°$; 40% NR; (P9175).**

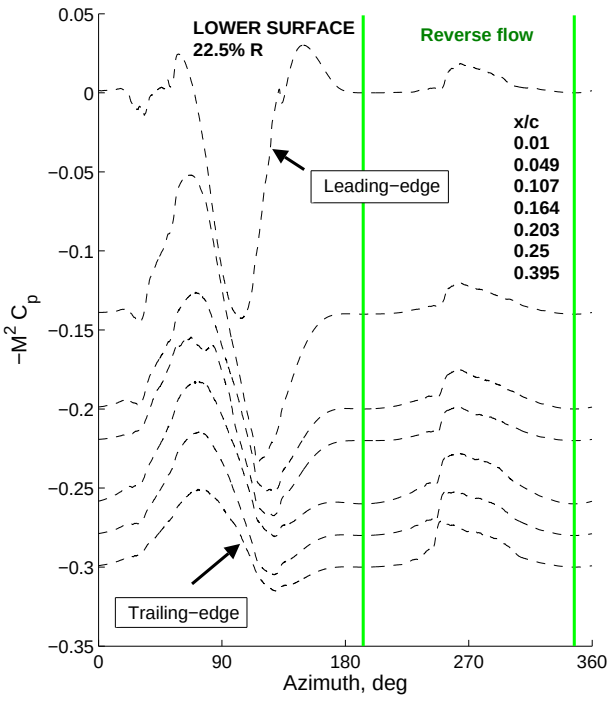

Figure 43: **Lower surface pressures at 22.5% R; $\mu = 1.0$; $C_T/\sigma = 0.022$ ($\theta_{75} = 2°$), $\alpha_S = 0°$; 40% NR; (P9175).**

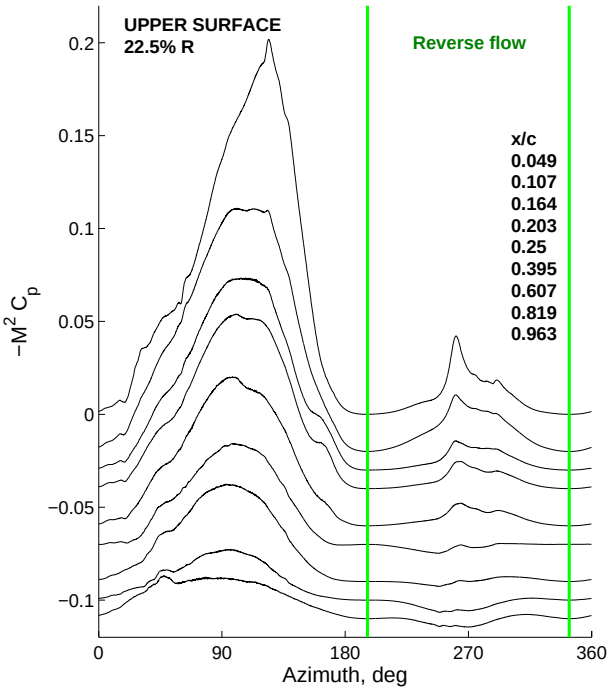

Figure 44: **Upper surface pressures at 22.5% R;** $\mu = 0.8$**;** $C_T/\sigma = 0.045$ $(\theta_{75} = 8°)$**,** $\alpha_S = 0°$**; 40% NR; (P9159).**

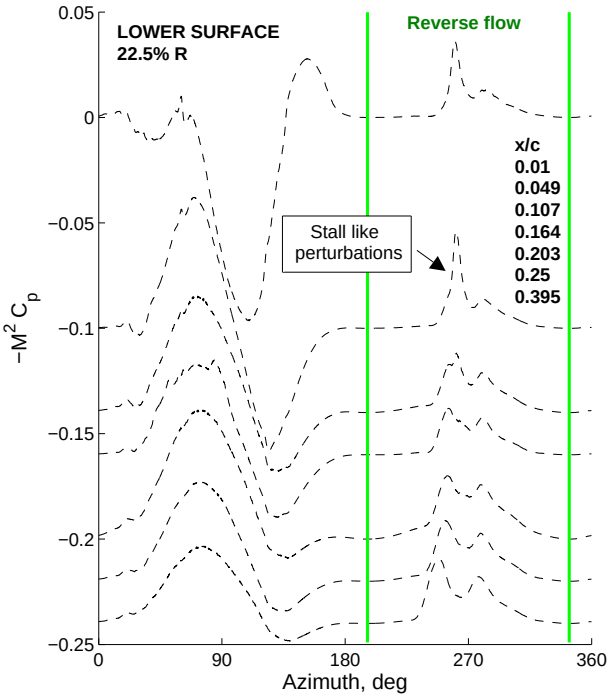

Figure 45: **Lower surface pressures at 22.5% R;** $\mu = 0.8$**;** $C_T/\sigma = 0.045$ $(\theta_{75} = 8°)$**,** $\alpha_S = 0°$**; 40% NR; (P9159).**

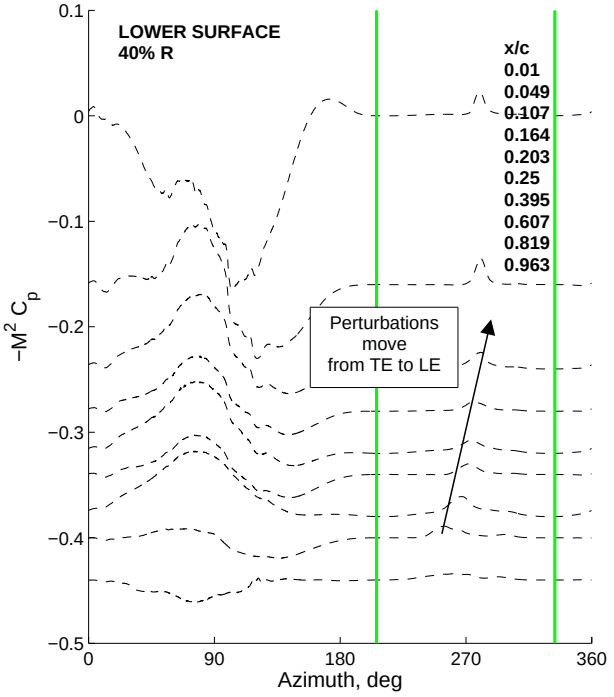

Figure 46: **Lower surface pressures at 40% R;** $\mu = 0.8$**;** $C_T/\sigma = 0.045$ $(\theta_{75} = 8°)$**,** $\alpha_S = 0°$**; 40% NR; (P9159).**

Figure 47: **Lower surface pressures at 40% R;** $\mu = 0.9$**;** $C_T/\sigma = 0.063$ $(\theta_{75} = 6.2°)$**,** $\alpha_S = 4°$**; 40% NR; (P9528).**

For confirmation, consider the test point: $\mu = 0.8$, $\alpha_S = 0°$, and $\theta_{75} = 8°$ (P9159). The reason for selecting this point is that the lower surface taps at 40%R are functional and cover up to very near the TE. (The upper surface taps are dysfunctional and prevent sectional integration). First, consider the upper and lower surface pressures at 22.5%R, Figs. 44 and 45. The advance ratio is lower in this flight, but because the collective angle is significantly higher, significant reverse flow effects are expected. The figures show that there is suction on both surfaces as before, but suction on the lower surface appears more marked. Compared to the previous point, the lower surface impulses are sharper and have a greater azimuthal movement. The impulse at 0.25c occurs at a slightly delayed azimuth compared to that at 0.395c, the impulse at 0.203c occurs at a slightly delayed azimuth compared to that at 0.25c, and so on. This is a signature of a stall vortex – a reverse chord stall vortex – triggered at the TE and sweeping across the lower surface in reverse chord direction towards the LE. The reason behind the double peak is not clear, but the the trailing edge being sharp it is possible that two vortices are formed one after the other. The azimuthal motion is negligible as the span location is very inboard. Next, consider the lower surface pressures at 40%R, Fig. 46. The reverse chord stall vortex appears clearly at this station as well and displays a wider azimuthal movement. However, there appears to be no distinct suction peak near the TE in the retreating side. Thus, the precise mechanism that triggers this vortex is not clear. It is clear however, that these peaks are responsible for the retreating side impulse in sectional pitching moments shown later in Fig. 54 and the torsion loads shown earlier Figs. 32 and 35.

Consider the test point: $\mu = 0.9$, $\alpha_S = 4°$, and $\theta_{75} = 6.2°$ (P9528). The shaft angle is higher here and consequently the reverse flow is expected to be less severe. The reason for selecting this point is that the lower surface taps at 67.5%R are functional, and allow insights into the flow field at a further outboard blade station. First, the lower surface pressures at 40%R, Fig. 47, confirm that pattern is similar to that of the previous point, although the reverse chord stall vortex is weaker as expected. The pressures at 67.5% R are shown in Fig. 48. The reverse flow region appears tranquil – with no unsteady airloading – indicating the possibility of a completely separated flow. This is examined more closely in Fig. 49 where the chordwise variation of lower surface pressures (C_p) are compared at several azimuthal locations covering the advancing and retreating sides. The advancing side experiences a high suction near the LE, Fig. 49(a). The retreating side, Fig. 49(b), shows greater suction near the TE, but the pressure levels are negligible compared to the advancing side. This again suggests a fully separated flow. On the advancing side, high suction indicates significant flow accelerations accompanied by the onset of local supersonic flow. The estimated azimuthal extent of the supersonic flow is demarcated in Fig. 48 by the intersection of the sonic line (Eq. 8 with $M_l = 1.0$) with the pressure lines. (Henceforth only the intersections are shown indicating the onset and recovery). Only the LE (within 1% chord) experiences supersonic flow at this station.

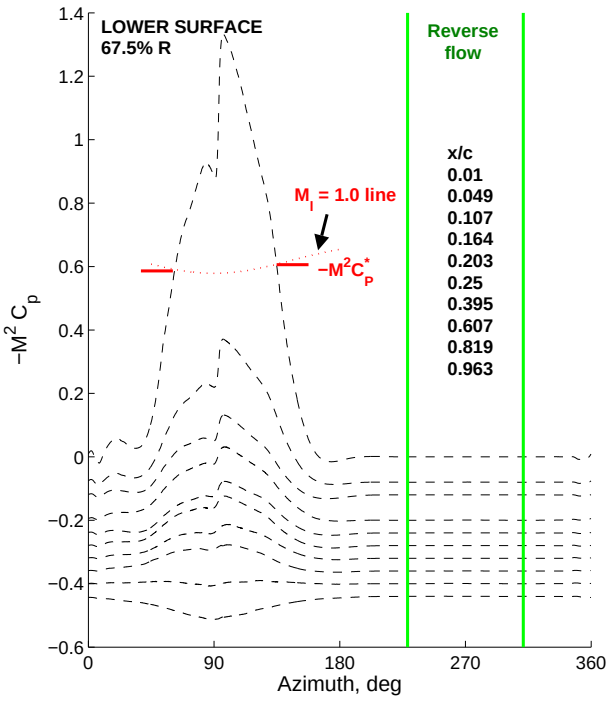

Figure 48: **Lower surface pressures at 67.5% R;** $\mu = 0.9$**;** $C_T/\sigma = 0.063$ ($\theta_{75} = 6.2°$)**,** $\alpha_S = 4°$**; 40% NR; (P9528).**

In order to examine stations further outboard, consider the highest advance ratio point again: $\mu = 1.0$, $\theta_{75} = 1.9°$, and $\alpha_S = 0°$ (P9175). The pressures at 77.5% R are shown in Figs. 50 and 51. Similar to the 67.5% R station of the previous point, the reverse flow region in the retreating side at this point also appears tranquil, and like before, the lower surface of the advancing side reveals significant supersonic flow. The same remains true further outboard at 86.5% R, see Figs. 52 and 53. At this station more than 10% of the LE experiences supersonic flow. Note that, the advancing tip Mach number M_A is only 0.52 (even without the cosine sweep factor), the thrust C_T/σ merely 0.022, and the longitudinal cyclic a meagre $-1.8°$. Local supersonic flow under such conditions appears to support the conjecture that the blades are carrying a very significant amount of elastic twist. This is further supported by the high negative loading seen in the sectional airloads at this station.

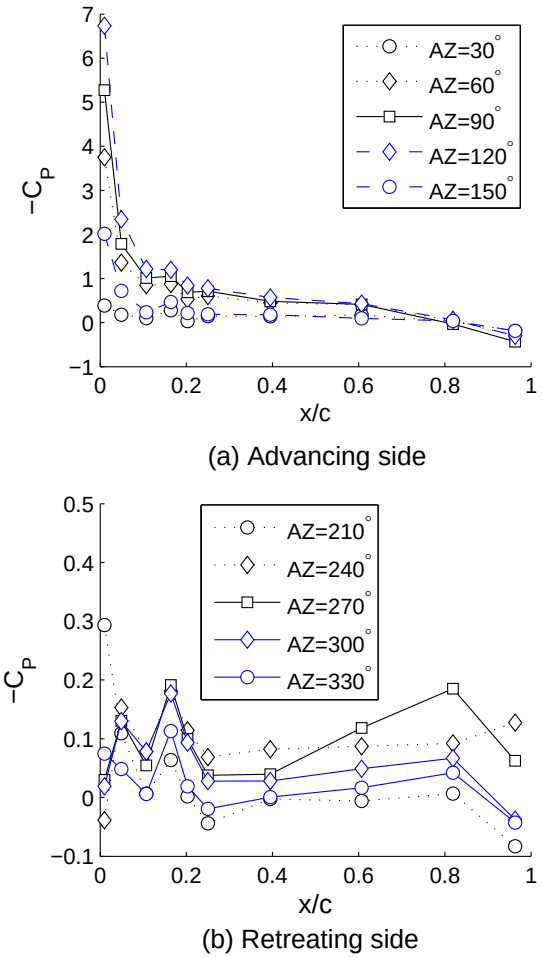

Figure 49: **Chord-wise pressures along 67.5% R lower surface on advancing and retreating sides;** $\mu = 0.9$**;** $C_T/\sigma = 0.063$ $(\theta_{75} = 6.2°)$**,** $\alpha_S = 4°$**; 40% NR; (P9528).**

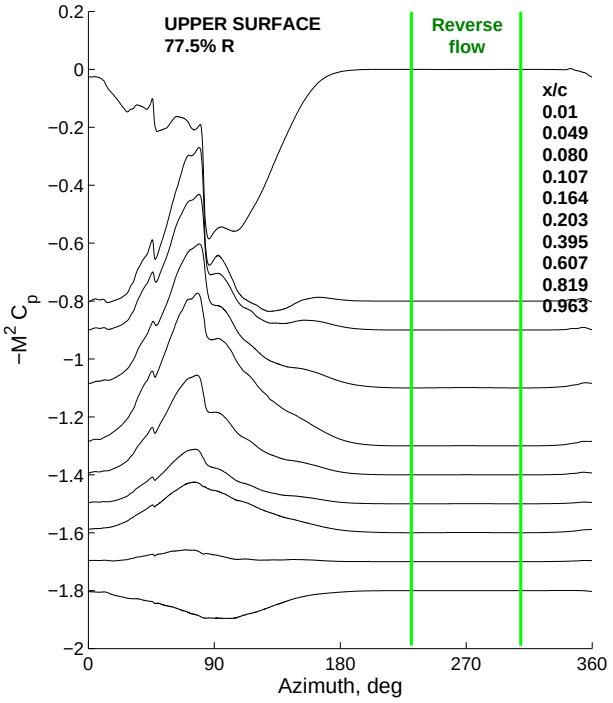

Figure 50: **Upper surface pressures at 77.5% R;** $\mu = 1.0$**;** $C_T/\sigma = 0.022$ $(\theta_{75} = 2°)$**,** $\alpha_S = 0°$**; 40% NR; (P9175).**

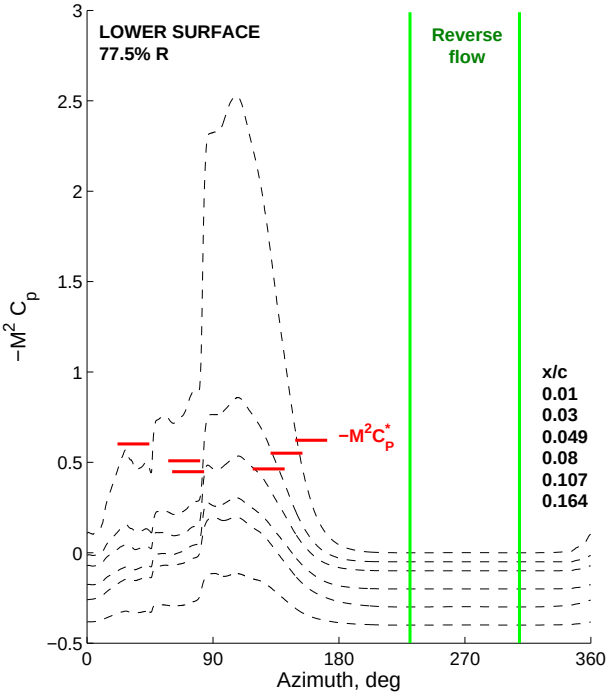

Figure 51: **Lower surface pressures at 77.5% R;** $\mu = 1.0$**;** $C_T/\sigma = 0.022$ $(\theta_{75} = 2°)$**,** $\alpha_S = 0°$**; 40% NR; (P9175).**

Figure 54 shows the inboard (22.5% R) and outboard (86.5% R) sectional airloads for the two high advance ratio conditions at $\mu = 0.8$ (characterized by reverse chord dynamic stall) and $\mu = 1.0$ (characterized by supersonic flow). The airloads are expressed in standard non-dimensional forms of forcing per unit span: M^2c_n, M^2c_c, and M^2c_m for normal force, chord force, and pitching moment about local 1/4-th chord. The inboard station (22.5% R) shows the reverse chord dynamic stall vortex impulse in the retreating side. The normal force increment (ΔM^2c_n) of about 0.05 and the associated nose up pitching moment increment (ΔM^2c_m) of about 0.0125 indicates that the reverse flow lift now acts roughly a further 1/4-c behind the local 1/4-c from the LE (i.e., at 1/2-c). Its contribution to chord force is substantial – the amplitude of the spike is by itself greater than the peak amplitude of chord force variation at the outboard station (86.5%

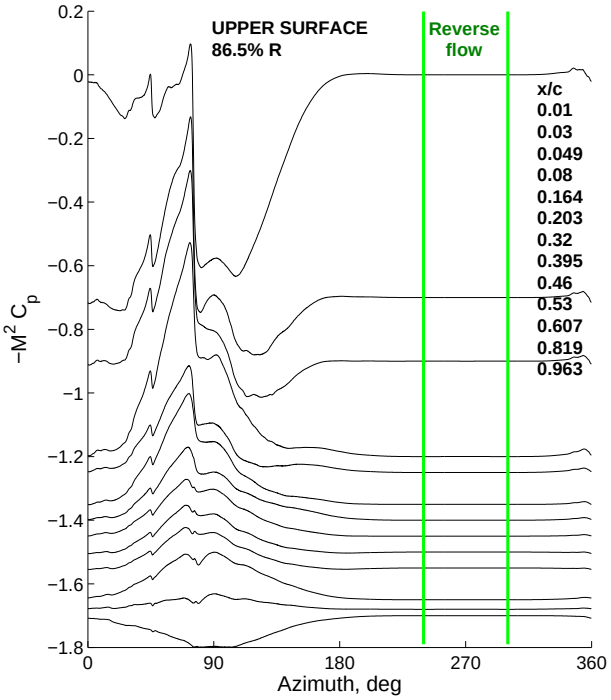

Figure 52: **Upper surface pressures at 86.5% R;** $\mu = 1.0$**;** $C_T/\sigma = 0.022$ $(\theta_{75} = 2°)$**,** $\alpha_S = 0°$**; 40% NR; (P9175).**

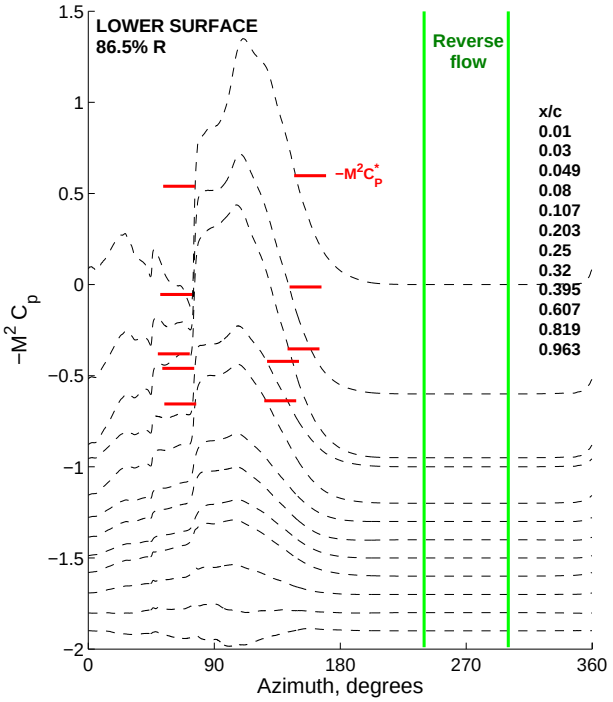

Figure 53: **Lower surface pressures at 86.5% R;** $\mu = 1.0$**;** $C_T/\sigma = 0.022$ $(\theta_{75} = 2°)$**,** $\alpha_S = 0°$**; 40% NR; (P9175).**

R). The outboard station (86.5% R) is immersed deeply into negative loading. At $\mu = 1.0$, almost the entire advancing side at this station carries a negative loading. The transonic pitching moments on the advancing side drive this negative loading via elastic twist.

Unlike nominal rotors, supersonic flow poses no danger of high speed impulsive noise in a slowed rotor. The sonic cylinder lies too far away from the tip for any likelihood of shock delocalization. The primary danger is that of excessive wave drag, and this is reflected in the high performance penalty (high -C_X) shown earlier in Fig. 21.

In summary, the retreating side lower surface shows evidence of reverse chord dynamic stall phenomena at the inboard stations (40% R and inboard) with the stall vortex sweeping from TE to LE. The advancing side lower surface shows evidence of supersonic flow at the outboard stations (67.5% R and outboard) even at subsonic advancing tip Mach numbers. The reverse chord dynamic stall inboard appears to be a key contributor to the retreating side impulse in torsion loading. The advancing side supersonic flow outboard appears to be a key contributor to large elastic twist deformations. The consequent high differential airloading immerses an outboard station (86.5% R) into negative lift on over the entire advancing side. The supersonic flow appears to be a significant contributor to the high drag penalty observed earlier in rotor performance.

SUMMARY AND CONCLUSIONS

A full-scale UH-60A rotor was tested at the NFAC 40- by 80- ft wind tunnel under slowed RPM (65% and 40% of nominal) reaching a maximum advance ratio of 1.0. Comprehensive measurements of performance, blade loads, hub loads, pressures/airloads were acquired. An initial examination of the measurements were presented with emphasis on the fundamental understanding of the aeromechanical phenomena unique to this regime. The intent was to gain useful knowledge for the design of high speed, high efficiency, slowed rotors of the future and acquire a challenging database for advanced analyses validation. Based on this research, on this specific rotor, the following conclusions are drawn:

1. The dynamic loads on the slowed rotor (bending and torsion moments and pitch link loads) operating at an advance ratio $\mu = 0.8$ and beyond, are comparable to or significantly greater than those encountered by the nominal rotor at its highest speeds. The net thrust level is not even a remote indicator of these load levels.

2. The primary reason behind the high dynamic loads

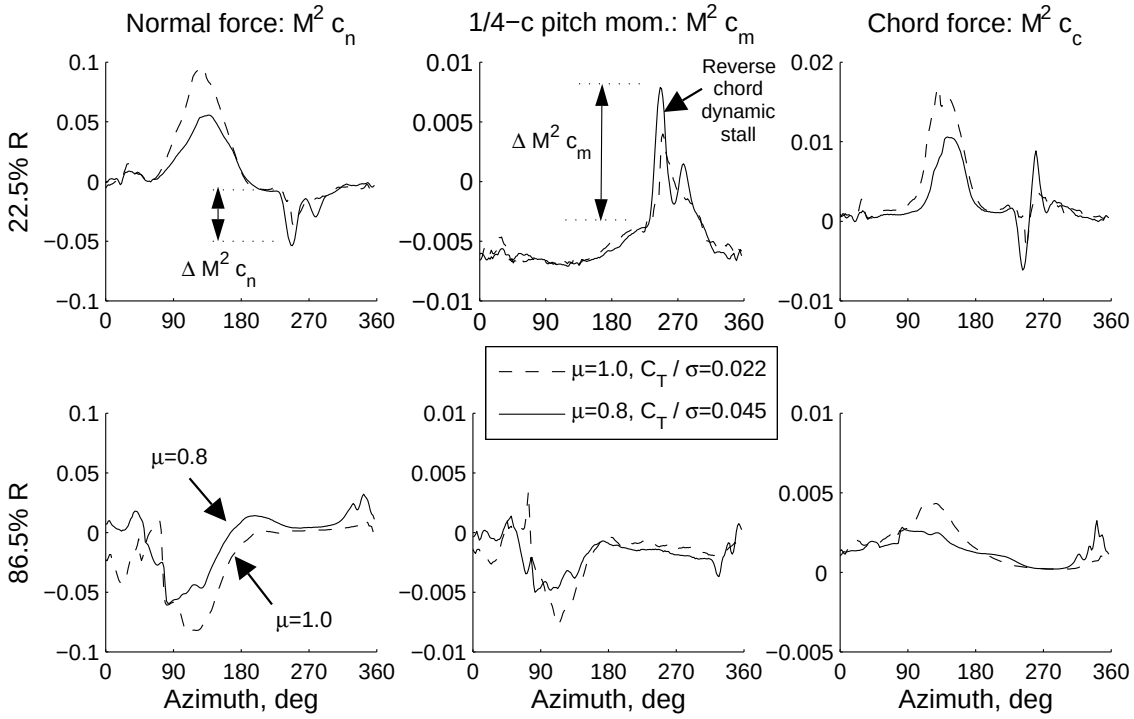

Figure 54: **Sectional airloads at 22.5% and 86.5% R for the 40% NR slowed rotor at two high advance ratio points:** $\mu = 1.0, C_T/\sigma = 0.022, \theta = 2°, \alpha_S = 0°$ **(P9175); and** $\mu = 0.8, C_T/\sigma = 0.045, \theta = 8°, \alpha_S = 0°$ **(P9159).**

appears to be a high differential airloading between the inboard and outboard sections of the advancing side. The requirement to achieve trim with large regions of negative (or zero) lift on the retreating side results in high longitudinal cyclic angles which, together with the high built-in twist, drives the lower surface of the advancing side to supersonic flow – even as inboard as 67.5%R. The resulting pitching moments generates very large elastic twist deformations that produces the differential airloading.

3. The large elastic twist drives the advancing blade outboard sections deep into negative lift. At $\mu = 1.0$ ($C_T/\sigma = 0.022$) the 86.5%R station is found negatively loaded over almost the entire first and second quadrants. These phenomena also appear to be an important driver behind thrust reversal. An increase in collective increases longitudinal cyclic which drives the elastic twist higher (see above) with little or no gain in net thrust.

4. The vibratory hub loads (dominantly 4P for this rotor) remains benign. The 4P vertical force is reduced by at least 50%. The 4P pitching moment is reduced by at least 50%–75% due to a dramatic reduction of 5P blade bending moments. This reduction is in turn caused by the wide rotor frequency gap between the second flap (3.33P) and first torsion (7.33P) modes.

5. The positively loaded (suction) lower surface of the retreating side reverse flow region shows evidence of reverse chord dynamic stall: vortices sweeping across the chord from trailing to leading edge. The absence of a distinct local suction acting as a trigger suggests a sharp trailing edge induced stall. Pressure spikes resembling multiple stall vortices are also observed at 22.5%R.

6. Other than the reverse chord dynamic stall phenomena the reverse flow region appears tranquil and does not contribute to any significant unsteady airloading.

7. At advance ratios beyond $\mu = 0.9$, the peak torsion loads are significantly affected by a nose up reverse flow impulse on the retreating side. It generally results from the downward lift and an aft center of pressure movement, but is significantly aggrevated by the onset of reverse chord dynamic stall.

8. The performance measurements were consistent with previous test data. The thrust reversal with collective angle at high advance ratios is observed as expected. The rotor is more efficient at a positive shaft angle, but at the expense of higher drag. It appears, that the large supersonic flow region on the lower surface of the advancing side is a key

contributor to the high drag even at low advancing tip Mach numbers.

ACKNOWLEDGEMENTS

The slowed rotor test was made possible by the collaborative efforts of the project partners – NASA and U. S. Army – as well as the U. S. Air Force's NFAC team. The authors acknowledge Sikorsky Aircraft's review and recommendations of the special motions and loads allowables for the test. The authors thank Wayne Johnson and Frank Harris for their involvement during test planning and preparation.

REFERENCES

[1] Rosen, K. M., "A Prospective: The Importance of Propulsion Technology to the Development of Helicopter Systems with a Vision for the Future, The 27th Alexander A. Nikolsky Lecture," *Journal of the American Helicopter Society*, Vol. 53, (4), October 2008, pp. 307–337.

[2] Stevens, M. A., Handschuh, R. F. and Lewicki, D. G., "Concepts for Variable/Multi-Speed Rotorcraft Drive System," NASA/TM-2008-215276, September 2008.

[3] Snyder, C. A., Robuck, M., Wilkerson, J., and Nordstrom, C., "Summary of the Large Civit Tiltrotor (LCTR2) Engine Gearbox Study," International Powered Lift Conference, Philadelphia, PA, October 5–7, 2010.

[4] Blackwell, R. and Millott, T., "Dynamic Design Characteristics of the Sikorsky X2 TD Aircraft," American Helicopter Society Annual Forum 64, Montreal, Canada, April 29 - May 1, 2008.

[5] Bagai, A., "Aerodynamic Design of the X2 TD Main Rotor," American Helicopter Society Annual Forum 64, , Montreal, Canada, April 29 - May 1, 2008.

[6] Karem, A. E., "Optimum Speed Rotor," U.S. Patent No. 6007298, December 28, 1999.

[7] Waide, W. M. and Karem, A. E., "Rotorcraft Engine and Rotor Speed Synchronization," U.S. Patent No. 7866598, January 11, 2011.

[8] Charnov, B. H., *From Autogiro to Gyroplane: The Amazing Survival of an Aviation Technology*, Praeger Publishers, Westport, CT, 2003.

[9] Marks, M. D., "Flight Test Development of XV-1 Convertiplane," American Helicopter Society Annual National Forum 3, Dallas, TX, October 8, 1956.

[10] Gibbings, D., "The Fairey Rotodyne - Technology Before Its Time ?", *The Aeronautical Journal*, 2003 Cierva Lecture, November 2004, Vol. 108, (1089), pp. 565–574.

[11] Robb, R. L., "Hybrid Helicopters: Compounding the Quest for Speed," *Vertiflight* magazine, Summer 2006, pp. 30–54.

[12] Ormiston, R. A., "Low-Disk Loading Compound Rotorcraft for High Speed and Aerodynamic Efficiency," AHS, AIAA, SAE, RAeS International Powered Lift Conference, October 5-7, 2010.

[13] Spreuer, W. E., "Experimental Flight Tests of the XH-51A Compound Helicopter," *Journal of the American Helicopter Society*, Vol. 13, (3), July 1969, pp. 64–69.

[14] Johnson, W., Yamauchi, G. K., and Watts, M. E., "NASA Heavy Lift Rotorcraft Systems Investigation," NASA TP 2005-213467, December 2005.

[15] Yeo, H. and Johnson, W., "Aeromechanics Analysis of a Heavy Lift Slowed-Rotor Compound Helicopter," *Journal of Aircraft*, Vol. 44, (2), March-April 2009, pp. 501–508.

[16] Floros, M. W. and Johnson, W., "Stability and Control Analysis of the Slowed-Rotor Compound Helicopter," *Journal of the American Helicopter Society*, Vol.52, (3), July 2007, pp. 239–253.

[17] Yeo, H. and Johnson, W., "Optimum Design of a Compound Helicopter," *Journal of Aircraft*, Vol. 46, (4), July-August 2009, pp. 1210–1221.

[18] Floros, M. W. and Johnson, W., "Performance Analysis of the Slowed-Rotor Compound Helicopter Configuration," *Journal of the American Helicopter Society*, 54, 022002 (2009).

[19] Ormiston, R. A. "Applications of the Induced Power Model and Performance of Conventional and Advanced Rotorcraft," American Helicopter Society Aeromechanics Specialists' Conference, San Francisco, CA, January 20-22, 2010.

[20] Walsh, D., Weiner, S., Arifian, K., Bagai, A., Lawrence, T., Blackwell, R., "Development Testing of the Sikorsky X2 TechnologyTM Demonstrator," AHS Annual Forum 65, Grapevine, TX, May 2009.

[21] Roesch, P., "Fast Hybrid Helicopter with Long Range with Longitudinal Trim Control," U.S. Patent No. 2010/0224720 A1, September 9, 2010.

[22] Eglin, P., "Drive Control and Regulation Method and System for a Hybrid Helicopter," U.S. Patent No. 2010/0310371 A1, December 9, 2010.

[23] Geiger, B., Piasecki, F. W., Horn, J. F., Lotterio, M., and Schifferle, P., "Challenges of Flight Control in a Compound Helicopter," AHS, AIAA, SAE, RAeS International Powered Lift Conference, October 5-7, 2010.

[24] Carter, J., "CarterCopter – A High Technology Gyroplane," American Helicopter Society Vertical Lift Design Conference, San Francisco CA, January 19–21, 2000.

[25] Wheatley, J. B. and Hood, M. L., "Full-Scale Wind-Tunnel Tests of a PCA-2 Autogiro Rotor," NACA Report No. 515, 1935.

[26] Jenkins Jr., J.L., "Wind-Tunnel Measurements on a Lifting Rotor at High Thrust Coefficients and High Tip-Speed Ratios," NASA-TN-D-2462, 1964.

[27] Jenkins Jr., J.L. "Wind Tunnel Investigation of a Lifting Rotor at Tip-Speed Ratios from 0.65 to 1.45," NASA TN D-2628, February 1965.

[28] McCloud III, J. L. and Biggers, J. C., "An Investigation of Full-Scale Helicopter Rotors At High Advance Ratios and Advancing Tip Mach Numbers," NASA TN D-4632, July 1968.

[29] Charles, B. D. and Tanner, W. H., "Wind Tunnel Investigation of Semirigid Full-Scale Rotors Operating at High Advance Ratios," USAAVLABS Technical Report 69-2, January 1969.

[30] Harris, F. D., "Rotor Performance at High Advance Ratio; Theory versus Test," NASA CR 2008-215370, October 2008.

[31] Quackenbush, T. R, Wachspress, D. A., McKillip, R. M. and Sibilia, M. J., "Experimental and Analytical Studies of Lifting Rotor Performance at High Advance Ratios," AHS Aeromechanics Specialists' Conference, San Francisco, CA, January 20-20, 2010.

[32] Berry, B. and Chopra, I., "Wind Tunnel Testing for Performance and Vibratory Loads of a Variable-Speed Mach-Scale Rotor" AHS Annual Forum 67, Virginia Beach, VA, May 3-5, 2011.

[33] Norman, T. R., Shinoda, P., Peterson, R. L. and Datta, A., "Full-Scale Wind Tunnel Test of The UH-60A Airloads Rotor," American Helicopter Society Annual Forum 67, May 3-5, Virginia Beach, VA, 2011.

[34] Kufeld, R. M., Balough, D. L., Cross, J. L., Studebaker, K. F., Jennison, C. D., and Bousman, W. G., "Flight Testing of the UH-60A Airloads Aircraft," American Helicopter Society Annual Forum 50, Washington D. C., May 1994.

[35] Olson, L. E., Abrego, A. I., Barrows, D. A., and Burner, A. W., "Blade Deflection Measurements of an Full-Scale UH-60A Rotor System," American Helicopter Society Aeromechanics Specialists' Conference, San Francisco, CA, January 20-22, 2010.

[36] Heineck, J. T., Schairer, E. T., Kushner, L. K., and Walker, L. A., " Retroreflective Background Oriented Schlieren (RBOS) as Applied to Full-Scale UH-60 Blade Tip Vortices," American Helicopter Society Aeromechanics Specialists' Conference, San Francisco, CA, January 20-22, 2010.

[37] Niebanck, C. F., "A Comparison of Dynamically Scaled Model Rotor Test Data with Discrete Azimuth Aeroelastic Stability Theory," American Helicopter Society Annual National Forum 25, Washington D.C., May 14-16, 1969.; see also: Ham, N. D., and Johnson, W., "A Comparison of Dynamically Scaled Model Rotor Test Data with Discrete Azimuth Aeroelastic Stability Theory," American Helicopter Society Annual National Forum 25, Washington D.C., May 14-16, 1969.